



Contents lists available at ScienceDirect

## Journal of the Mechanics and Physics of Solids

journal homepage: [www.elsevier.com/locate/jmps](http://www.elsevier.com/locate/jmps)

# Correlation between topology and elastic properties of imperfect truss-lattice materials



Andrew Gross<sup>a,1</sup>, Panos Pantidis<sup>b,1</sup>, Katia Bertoldi<sup>a,\*</sup>, Simos Gerasimidis<sup>b,\*</sup>

<sup>a</sup>John A. Paulson School of Engineering and Applied Sciences, Harvard University, Cambridge, MA, United States

<sup>b</sup>Department of Civil and Environmental Engineering, University of Massachusetts, Amherst, MA, United States

## ARTICLE INFO

### Article history:

Received 4 October 2018

Revised 9 November 2018

Accepted 10 November 2018

Available online 20 November 2018

### Keywords:

Architected-material

Topology

Truss-lattice

Micro-truss

Defect

Void

## ABSTRACT

Recent advances in additive manufacturing at small scales has revealed the exceptional mechanical properties that can be achieved by truss-lattice materials. This study investigates the response of four topologically distinct truss-lattice architectures to the inclusion of defects in order to elucidate how defects influence the elastic properties of these materials. Numerical results from finite element models of periodic beam networks with missing building blocks are compared to both analytical continuum models with a micromechanical basis and to experiments with characteristic feature sizes on the nano and micro scales. Notably, this comparison reveals that the elastic properties of highly connected lattice-truss materials respond to defects in the same manner as homogeneous materials.

© 2018 Elsevier Ltd. All rights reserved.

## 1. Introduction

The pursuit of new materials with properties superior to the current state of the art has led many investigators to examine the behavior of materials with feature sizes in the range of micrometers and nanometers. In the realm of mechanical properties, the motivation for diving to smaller scales originates with the observation that the strength of many materials can be dramatically dependent on their characteristic feature size (Griffith and Eng, 1921; Hall, 1951; Petch, 1953). The impact of these observations on material development over the last century is diverse and far reaching. Enabled by recent advances in small scale fabrication, the “smaller is stronger” principle has been reapplied in the setting of truss-lattice materials. Fabrication of these periodic strut networks at increasingly smaller scales has given rise to unique behavior such as ceramic materials that can sustain large deformations and low-density materials with record setting strength (Bauer et al., 2016; Meza et al., 2014; Schaedler et al., 2011). While there exists an array of top-down techniques for fabricating truss-lattice materials, two competing trends are nearly universal: (i) the mechanical performance of the material is inversely proportional to the length scale of the geometry and (ii) the scalability of material production is directly proportional to the length scale of the geometry.

One of the most promising pathways to simultaneously decrease the cost of production and the length scale of a truss-lattice material is to use self-assembly (bottom-up techniques). A variety of methods are viable candidates for this purpose. DNA origami has general techniques for the design and fabrication of three-dimensional structures with few limitations

\* Corresponding authors.

E-mail addresses: [bertoldi@seas.harvard.edu](mailto:bertoldi@seas.harvard.edu) (K. Bertoldi), [sgerasimidis@umass.edu](mailto:sgerasimidis@umass.edu) (S. Gerasimidis).

<sup>1</sup> These authors contributed equally.

on geometric complexity (Douglas et al., 2009b; Winfree et al., 1998). Block copolymer self-assembly can transform simple ingredients into a variety of complex geometric patterns with high throughput (Hajduk et al., 1994). Colloidal crystals can be synthesized in large volumes from constituents spanning orders of magnitude in length scale to form hierarchical materials (Wang et al., 2006). These are just a few examples from a plethora of promising bottom-up techniques and variants that continue to rapidly develop.

Defects of various forms and concentrations are unavoidable with any fabrication route. Although approaches have been developed to dramatically reduce errors in self-assembly, the most effective techniques are typically driven by interaction with a templated surface (Kim et al., 2003; Van Blaaderen et al., 1997). It is anticipated that the application of self-assembly techniques to larger three-dimensional volumes will also increase the frequency of defects in the resulting architected-material. Of particular interest for the self-assembly of truss-lattice materials is the influence of struts that are missing from the network. Missing building blocks have been observed in the products of multiple self-assembly techniques (Douglas et al., 2009a; Ye et al., 2001), and missing struts have been singled out as the most severe defect in reducing the strength of a truss-lattice (Chen et al., 1999). Several investigations have examined the effect of various defect types (including the perturbation of nodal positions, initial waviness of struts, struts with non-constant cross sectional area, random removal of struts, and clustered removal of struts) on the elastic, yield, buckling, localization, and collapse behavior for a variety of two-dimensional truss-lattice materials (Guo et al., 1994; Guo and Gibson, 1999; Silva and Gibson, 1997; Symons and Fleck, 2008). However, corresponding studies on the effect of defects on the properties of three-dimensional truss-lattice materials have been less extensive (Lu et al., 2011; Wallach and Gibson, 2001). Furthermore, the connection between defect containing truss-lattice materials and well established techniques for the homogenization of Cauchy continua has been even less explored. Application of these micromechanically rooted methods for the calculation of macroscopic properties, such as those covered by Nemat-Nasser and Hori (2013) and Mura (2013), to truss-lattice materials is essentially absent from the literature. The only bridge between the mature topics of micromechanical homogenization and truss-lattice materials exists as an extension of micromechanics based homogenization applied to the discrete microstructure of a two-dimensional triangular lattice (Liu and Liang, 2012). While this past work is unique in addressing the topic of physical models for defect containing truss-lattice materials, additional interpretation of the model results is necessary to reveal the true nature of these materials. In particular, their suggestion that the Hashin–Shtrikman upper-bound lies far above the true least upper-bound for a highly connected truss-lattice appears inconsistent with the current work.

In this study, the dependence of the elastic moduli on the concentration and distribution of missing struts is investigated for several three-dimensional truss-lattice materials of varying coordination number. To begin, observations from a demonstrative experiment show how the elastic response of a truss-lattice material to the inclusion of voids is architecture dependent. Next, a finite element investigation utilizing beam models is used to calculate the degradation of the elastic properties for truss-lattice materials that contain voids of various size, volume fraction, and arrangement. A comparison of these results to those from analytical models for isotropic homogeneous materials that contain similar defects show excellent correspondence between the two approaches for topologies that are highly connected. Two of the architectures with designed defects are then fabricated using two-photon polymerization and tested under uniaxial compression to provide experimental verification. A similar numerical, analytical, experimental investigation is then conducted for truss-lattice materials that contain randomly distributed defects. As a whole, the numerical and analytical approaches reveal that highly-connected lattice-truss materials respond to defects in the same manner as homogeneous materials, with the experiments demonstrating that this newly discovered characteristic can be realized in practice.

## 2. Experiments

To first probe the behavior of truss-lattice materials with defects, two architectures with differing coordination numbers,  $Z$ , were selected: the tetrakaidecahedron ( $Z = 4$ ) and the octet ( $Z = 12$ ). A detailed description of each architecture is provided in Section 3.1. The specimens were fabricated with two-photon lithography (Nanoscribe gmbh) in order to have feature sizes as close as possible to the length scale most common to self-assembly techniques, albeit still about one order of magnitude larger. Two-photon lithography was performed in the DiLL configuration with IP-Dip photoresist. After patterning, the specimens were developed in PGMEA (Baker BTS-220) for 20 minutes, followed by 5 minutes in IPA (J.T. Baker), and super-critical point  $\text{CO}_2$  drying. Note that a foundation is used to couple the specimens to the silicon substrate so that shrinkage that occurs during development does not distort the lattices. Moreover, to facilitate compression testing, a platen is fabricated on the top of each lattice. Following two-photon lithography, the polymer specimens are coated with  $\text{Al}_2\text{O}_3$  in order to ensure consistent material properties throughout each specimen and between specimens.  $\text{Al}_2\text{O}_3$  is deposited over the course of 500 atomic layer deposition cycles using TMA and DI water as precursors. Measurement of the coating thickness on the substrate with a scanning ellipsometer (Gaertner Scientific, LSE-W) indicates that  $58.5 \pm 0.4$  nm of  $\text{Al}_2\text{O}_3$  was deposited. Postmortem scanning electron microscope (SEM) images suggest that the deposition rate of  $\text{Al}_2\text{O}_3$  on the polymer specimens is nearly identical to that on the silicon substrate.

For each of the two truss-lattice architectures, pristine and voided structures based on a  $9 \times 9 \times 9$  tessellation of unit cells were fabricated. Fig. 1a and b show experimental specimens of pristine tetrakaidecahedron ( $Z = 4$ ) and octet truss-lattices ( $Z = 12$ ), respectively. The struts in both truss-lattice topologies are  $4.75 \mu\text{m}$  long and are elliptical in cross section with major and minor diameters of  $1140$  and  $555 \pm 15$  nm, respectively (see zoom-in view of an octet specimen in Fig. 1c). The choice of fabricating each specimen with equal size struts (resulting in relative density  $\bar{\rho} = 0.148$  and  $0.0206$  for the pristine

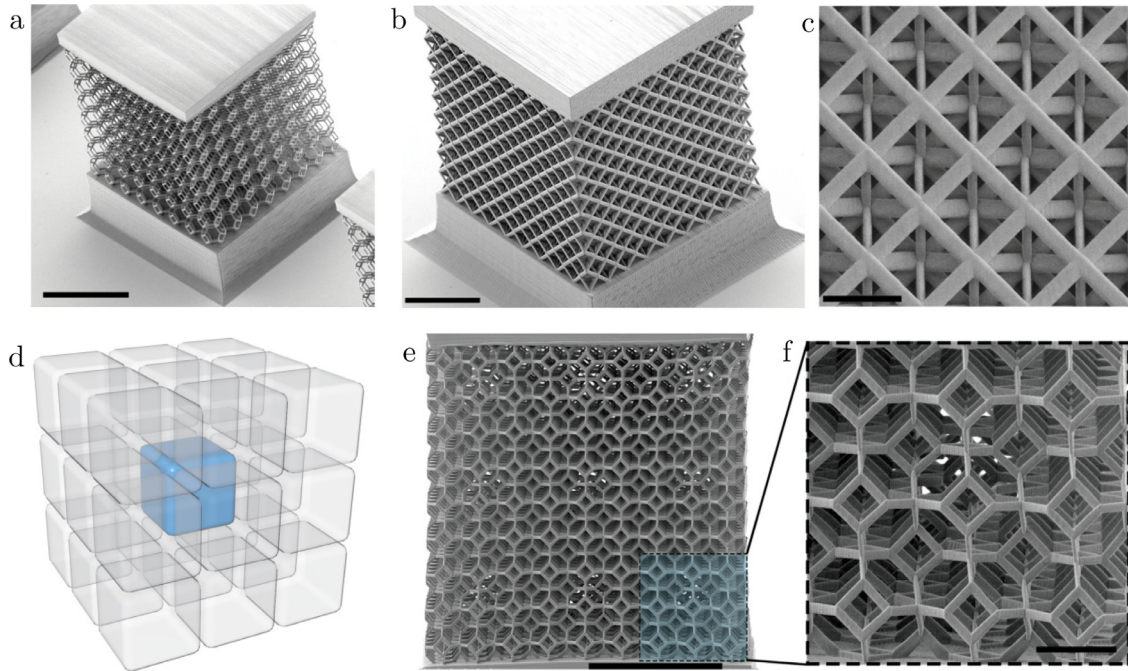


**Fig. 1.** (a). Oblique view of a tetrakaidecahedron truss-lattice experimental specimen with an  $8 \times 8 \times 8$  tessellation. The specimen is fabricated on a foundation to mitigate distortion from post-fabrication shrinkage, and a block adhered to the top of the specimen provides a well-defined boundary condition.  $50\mu\text{m}$  scale bar. (b). Oblique view of an octet truss-lattice experimental specimen with a  $9 \times 9 \times 9$  tessellation ( $20\mu\text{m}$  scale bar). (c). Normal view focusing on 9 octet unit cells ( $5\mu\text{m}$  scale bar). (d). Schematic of a supercell that consists of a  $3 \times 3 \times 3$  tessellation of unit cells with the central unit cell removed (colored blue). (e). Normal view of a voided tetrakaidecahedron truss-lattice experimental specimen ( $50\mu\text{m}$  scale bar). (f). High magnification image focused near one of the voids located within e. The struts removed to form the void are visible near the center of the image ( $10\mu\text{m}$  scale bar). (For interpretation of the references to color in this figure legend, the reader is referred to the web version of this article.)

octet and tetrakaidecahedron specimens, respectively<sup>2</sup>) is motivated by the goal of observing differences in behavior that are dominated by topology rather than geometry. For the specimens containing voids, 27 regularly spaced unit cells were removed to form a simple cubic arrangement of voids within the specimens. This can be visualized as a  $3 \times 3 \times 3$  tessellation of the supercell depicted in Fig. 1d. The voided tetrakaidecahedron truss-lattice is shown in Fig. 1e and f. The presence of the voids can be seen in regions where there appears to be light filtering in from behind the lattice.

Mechanical testing of the specimens were performed with an in-situ SEM nano-indenter (Femto Tools). The displacement is applied by a linear piezo flexure stage with capacitive position encoders and the reaction force is measured by a MEMS capacitive force sensor with a resolution of  $0.05\mu\text{N}$ . Five load cycles are applied in the linear elastic range, with the stopping criteria for the tests being when the load reaches 50% of the value at which the relationship between load and displacement ceases to be linear for a pristine specimen of the same architecture. The stress-strain response from compression testing of both lattice topologies with and without voids are shown in Fig. 2a.<sup>3</sup> All stress-strain curves are nearly linear, with only a slight non-linearity apparent in the curves for the octet specimens. This is likely due to a slight misalignment between the indenter and specimen, causing an increase in contact area (i.e. stiffer contact) as loading increases. Note that non-linearity from imperfect contact is expected to be most apparent for the octet specimens, as the compliance of these specimens and of imperfect contact are of comparable magnitude. To quantify the stiffness of the samples, their modulus of elasticity,  $E$ , is calculated by performing a least squares linear fit to the upper half of the load range applied to each specimen. Consistent with results from the literature, the specific modulus  $\bar{E} = E/\bar{\rho}$  for the octet is found to be significantly larger than that for tetrakaidecahedron (see Fig. 2b). As expected, when voids are introduced, a reduction in stiffness for both architectures is apparent in the stress-strain response. However, our results surprisingly reveal that the effect of the voids on the specific modulus of the two structures is substantially different, even for a relatively low volume fraction  $f = 0.037$ . While the reduction in specific modulus for the tetrakaidecahedron truss-lattice is about 7.7%, that for the octet truss-lattice is substantially smaller, at 2.1%.

<sup>2</sup> Note that these values of relative density are computed by CAD models using the as manufactured dimensions of the experimental specimens.

<sup>3</sup> Note that the strain is calculated using the relative displacement between the indenter and substrate (corrected to account for the compliance of the loading device and the specimen shoulders), while the stress is obtained by dividing the reaction force by the cross-sectional area of the structure in the undeformed configuration.

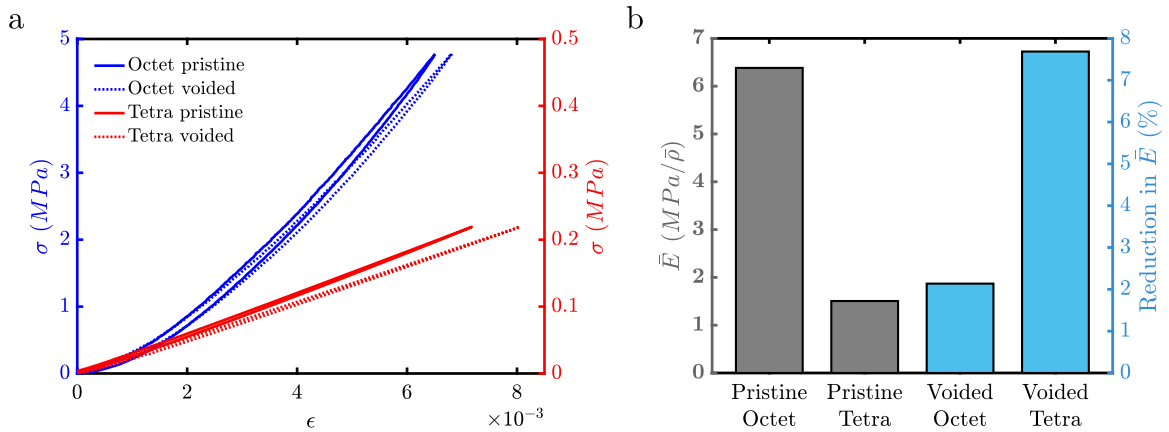


**Fig. 2.** (a). Stress-strain response from a single loading-unloading cycle for octet and tetra truss-lattice experimental specimens. Note that the tetra truss-lattice curves are plotted with respect to the right side y-axis values. (b). Experimentally measured specific elastic modulus,  $\bar{E}$ , of the pristine architectures and the reduction in specific modulus arising from a simple cubic arrangement of voids at a void volume fraction  $f = 0.035$ .

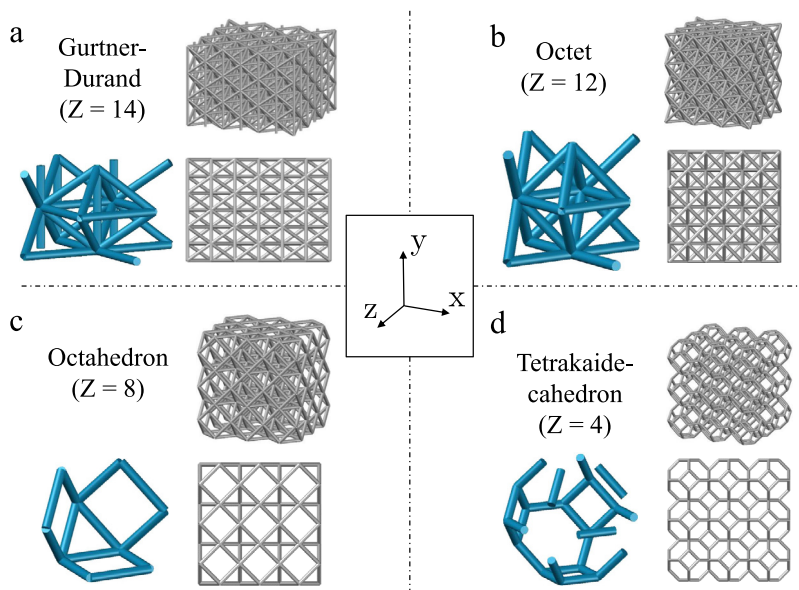


**Fig. 3.** Depiction of the unit cells used in this study, as well as side and 3D views of a  $3 \times 3 \times 3$  tessellation of unit cells for the (a). Gurtner–Durand, (b). octet, (c). octahedron, and (d). tetra truss-lattice architectures. (For interpretation of the references to color in the text, the reader is referred to the web version of this article.)

### 3. Analysis

The experimental results clearly indicate that architecture strongly affects how a truss-lattice responds to defects. Motivated by this observation, the link between topology and response to defects is further explored by examining numerical models of four truss-lattice architectures with varying coordination number. The cases of clustered defects (voids) and randomly distributed defects will be examined.

#### 3.1. Architectures

CAD models of the four architectures examined in this study are shown in Fig. 3. For each architecture the unit cell is shown in light blue color, while a 3D and side view of a  $3 \times 3 \times 3$  tessellation are shown in gray color. All of these architectures exhibit cubic symmetry and have similarly situated nodes. The tetra truss-lattice architecture is the least connected network considered, with a coordination number  $Z = 4$ , and can be categorized as a non-rigid bending-dominated material. The octahedron architecture has  $Z = 8$  and is a rigid bending-dominated material. The octet architecture has  $Z = 12$ , and is rigid stretching-dominated material. The recently proposed architecture by Gurtner and Durand (2014) has  $Z =$

**Table 1**

General properties and classifications of the truss-lattice architectures investigated. The relative densities are approximations made by neglecting the overlap between struts near nodes and correspond to a strut aspect ratio equal to  $\lambda = 20$ .

Architecture	Z	$\bar{\rho}$	Maxwell's criterion	Deformation
Tetrakaidecahedron	4	0.00833	Non-rigid	Bending
Octahedron	8	0.0333	Rigid	Bending
Octet	12	0.0666	Rigid	Stretching
Gurtner–Durand	14	0.0833	Rigid	Stretching

14, and is a rigid stretching-dominated material (see Table 1). All of the architectures can be represented within a cubic unit cell other than the Gurtner–Durand. This architecture was originally described within a tetrakaidecahedral unit cell, however a tetragonal unit cell is used here to emphasize the similarity between the Gurtner–Durand, octet, and octahedron architectures. Note that the planes of cubic symmetry are parallel to the faces of the unit cell for all unit-cell selections other than the unit cell used here for the Gurtner–Durand architecture. For this architecture the symmetry planes are normal to the vectors  $(1, 0, 1)$ ,  $(1, 0, -1)$ , and  $(0, 1, 0)$ , using the coordinate system defined in Fig. 3. Finally, the Gurtner–Durand architecture is the only architecture which possesses struts that are not all of equal length, and consists of two distinct families of struts, with uniform length and cross-section existing within each family.

To maintain consistency between the numerical and experimental aspects of this investigation, the geometric parameters of the strut cross-sections used for each architecture in the numerical analysis were selected to be compatible with the natural fabrication abilities of two-photon lithography. Thus, members of the truss-lattice possess an elliptical cross-section with a major axis that is twice the length of the minor axis, elongating the cross-section in the y-direction for all struts.<sup>4</sup> The elliptical cross-section lowers the level of symmetry for the materials from cubic to orthotropic. In the numerical investigation the strut aspect ratio,  $\lambda$ , is defined as the ratio of the axial to cross-sectional length of a strut,<sup>5</sup> is set to  $\lambda = 19.17$  for all architectures. Using the same strut aspect ratio for all architectures emphasizes topological effects over geometric, and results in a different  $\bar{\rho}$  for each architecture (see Table 1). Since the Gurtner–Durand architecture has two families of equal length struts, the average strut aspect ratio was set to  $\lambda = 19.17$ . In addition to this constraint, each strut was set to occupy the same volume, irrespective of which family it belongs to. The latter constraint allows the change in relative density from strut removal to be determined by the number of struts removed alone, without having to consider which family they belong to. It should be noted that the Gurtner–Durand architecture was originally proposed with different cross-sectional dimensions for the two families of struts, chosen specifically so that the architecture yields maximal stiffness and isotropy. To achieve these often desirable properties the ratio between the cross-sectional areas of the shorter family of struts to the longer must be  $9/8$ . Although we slightly modify this area ratio to be  $2/\sqrt{3}$ , we still refer to this modified design as the Gurtner–Durand architecture since these investigators first proposed this particular arrangement of struts, which we preserve.

### 3.2. Numerical analysis

Numerical models were analyzed using the finite element method (ABAQUS / Standard). All struts were discretized as Timoshenko beam elements with one integration point per element (ABAQUS element type B31). A mesh convergence study revealed that a single element per strut was sufficient to characterize the small deformation elastic properties for the Gurtner–Durand, octet, and octahedron architectures. Five elements per strut were found to be required for the tetrakaidecahedron architecture, likely due to the substantial bending deformations that are generated in this architecture. All finite element models consist of a suitably sized supercell with periodic boundary conditions applied. For all architectures and defect patterns investigated (other than non-uniform void distributions), three elastic moduli were calculated. Calculation of the bulk, shear, and Young's modulus were carried out by considering the strain energy stored within the supercell when subjected to the following loading states: hydrostatic pressure, shear strain, and uniaxial stress, respectively. In all simulations, only the small deformation elastic behavior was considered, thus material and geometric nonlinearities do not play a role.

#### 3.2.1. Truss-lattices with periodic voids

To investigate the effect of periodically distributed voids on the truss-lattice architectures, the properties of supercells comprised of  $N \times N \times N$  unit-cells with  $p$  voids of size  $n \times n \times n$  unit cells are calculated (using the unit cell definitions given in Fig. 3). With this description of a voided material, the void configuration of any architecture depends on three parameters: (i) the size of a void relative to the size of the unit-cell (defined by  $n$ ); (ii) the void volume fraction,  $f = pn^3/N^3$ ; (iii) the relative position of the voids. For the case  $p = 1$ , subsequently referred to as the case of uniformly distributed voids, the

<sup>4</sup> One exception exists for the struts that are parallel to the y-direction in the Gurtner–Durand architecture. For these struts the major axis is assigned to be in the z-direction.

<sup>5</sup> The cross-sectional length is taken to be the radius of the circle that has the same area as the cross-section.

**Table 2**

Elastic properties of the intact truss-lattice architectures considered in this study, calculated for struts that have an aspect ratio  $\lambda = 19.17$  and are composed of a parent material that has an elastic modulus of 2000 and a Poisson's ratio of 0.3. For excluded elastic constants, the following equalities exist:  $C_{3333} = C_{1111}$ ,  $C_{2233} = C_{1122}$ , and  $C_{2323} = C_{1212}$ , except for the Gurtner-Durand, where  $C_{2323} = 12.3$  as a result of the orientation chosen for the elliptical cross-section on struts that are parallel to the  $y$ -direction. The universal anisotropy index,  $A^U$ , is provided as well. The bulk modulus can be calculated as  $K = C_{ijj}/9$ .

Architecture	$C_{1111}$	$C_{2222}$	$C_{1122}$	$C_{1133}$	$C_{1212}$	$C_{3131}$	$A^U$
Tetrakaidecahedron	2.06	2.10	1.97	2.01	0.0317	0.0172	0.988
Octahedron	12.3	12.4	5.91	6.00	6.09	6.07	0.524
Octet	24.5	24.7	11.8	12.0	12.3	12.2	0.531
Gurtner-Durand	37.9	39.7	11.7	13.4	12.2	13.7	0.0180

voids will fall on a simple-cubic lattice for all architectures that are defined on a cubic unit cell. For the Gurtner–Durand architecture the voids are located on a tetragonal lattice when  $p = 1$ . For  $p > 1$  the distribution of voids will subsequently be referred to as non-uniform, since the difference between the nearest and second nearest neighbor distances for a void can vary substantially in this case. The subsequent section will report the results of numerical simulations conducted to explore the effect of each of the three parameters that define the voided geometry.

### 3.2.2. Truss-lattices with randomly excluded struts

Since the geometry of a truss-lattice material with randomly excluded struts is non-deterministic, its behavior is estimated through the concept of the stochastic volume element (SVE) (Ostoja-Starzewski, 2006). Two well-established criteria need to be satisfied in order to obtain the property of a material that is independent from the property of the finite domain size and realization of the random field applied to that domain. The first criterion, *spatial averaging*, requires a sufficiently large supercell to be investigated. If the supercell is too small then the periodicity of the randomly excluded struts will cause an error in the estimate. The second criterion, *ensemble averaging* requires the investigation of a sufficiently large set of random defect realizations. The combination of spatial and ensemble averaging allows for an efficient and accurate estimate of the average properties for a stochastic material (Kanit et al., 2003; Ostoja-Starzewski, 2006). In this study, preliminary analyses for the Young's modulus of the octet architecture with  $f = 0.15$  were performed with supercell sizes  $N = 6, 7$  and  $8$ , where in the context of random defects  $f$  is the fraction of struts that are selected for exclusion. For each supercell size, ensemble averaging was performed on a set of 1000 random realizations of excluded struts. All three supercell sizes considered returned same mean value for the Young's modulus within 0.01%. Although larger than required for the octet architecture, the supercell size  $N = 8$  was selected for all numerical models with random defects. This allows for a consistent supercell size across all architectures, while also allowing for the possibility that other architectures may require larger supercell sizes than the octet for convergence.

### 3.3. Elastic micromechanical models

A number of analytical models with a micromechanical basis have been developed to describe the homogenized elastic behavior of materials with multiple phases of homogeneous constituents (Mura, 2013; Nemat-Nasser and Hori, 2013). Even though these models have no ability to capture topological effects (i.e. the coordination number  $Z$  is disregarded, as the material is assumed to be continuous), in this study they are adopted to interpret the behavior of defect containing truss-lattice materials and provide further insights into their elastic response. To this end, the homogenized elastic response of the pristine truss-lattice materials is first characterized (see Table 2). This behavior, along with the defect volume fraction, is then used as an input to a suitable analytical model which provides an estimate of the homogenized properties of the defected medium. It should be noted that, for the sake of simplicity, analytical solutions for initially isotropic materials are used to predict the response of the defected orthotropic architectures considered in this investigation. As such, there exists a choice for which two elastic constants calculated for the pristine architectures should be selected as inputs to the elasticity solution. For this purpose, the bulk modulus is an obvious choice due to its orientation independence. For the other selected elastic constant, orientation cannot be avoided, so the shear modulus that corresponds to the component of shear deformation that is queried in Fig. 4c is selected. The selected shear modulus is identical to the elastic constant  $C_{1212}$  reported in Table 2 for each architecture. Additionally, it is important to point out that in order to maintain consistency in application of the analytical models the shape of all the defects is assumed to be spherical, introducing an additional approximation. However, despite all these simplifications, the comparison between the predictions of the analytical models and the numerical results are sufficiently informative to support the scope of this investigation.

As described in the remaining part of this section, analytical models are presented for lattices with uniformly distributed voids (i.e.  $p = 1$ ) and randomly excluded struts. In contrast, the case of multiple voids with arbitrary relative position within a unit cell (i.e.  $p = 2$ ) is examined with only numerical analyses and experiments, since micromechanical models are not readily available for this type of defect.

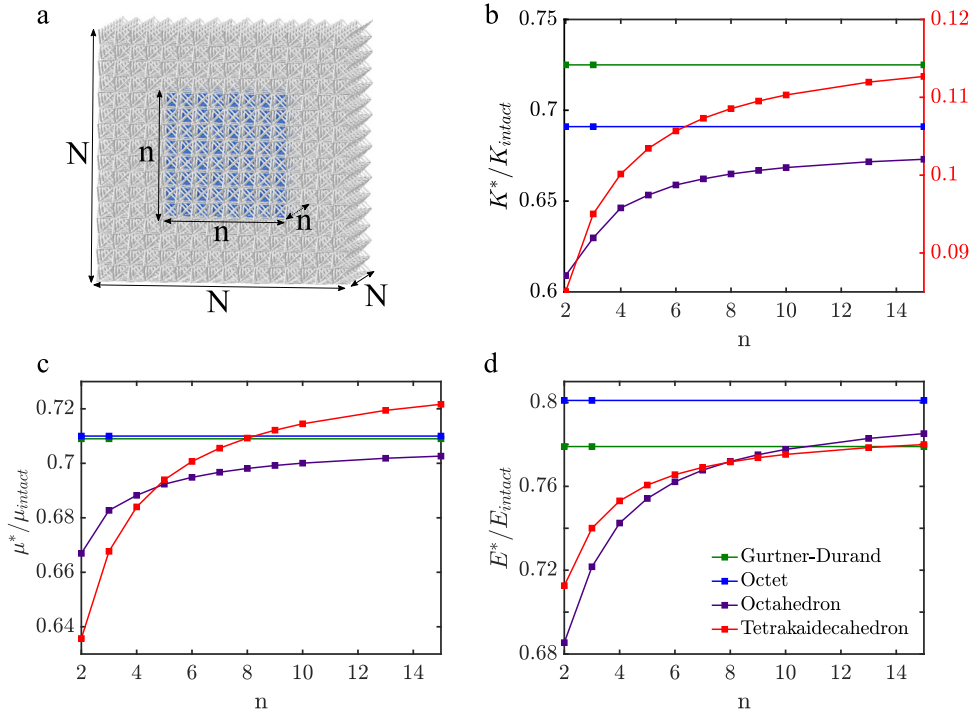


**Fig. 4.** (a). Schematic representation of an octet supercell of size  $N = 8$  and a void of size  $n = 4$ . (b-d). Dependency of the b. bulk modulus (note that the curve for the tetrakaidecahedron is plotted with respect to the right side y-axis values.), (c). shear modulus, and (d). Young's modulus on the void size relative to the unit-cell size of the architecture for uniformly distributed voids at a volume fraction of  $f = 0.125$ . The horizontal curves for the octet and Gurtner-Durand architectures indicate their insensitivity to void size.

### 3.3.1. Truss-lattices with periodic voids

To analytically predict the response of truss-lattices with uniformly-spaced voids, we consider spherical voids of radius  $R$  occupying the domain  $\Omega$  on a simple cubic lattice<sup>6</sup> with lattice constant  $\Lambda = (4\pi R^3/3f)^{1/3}$ . Under these assumptions, the effective bulk modulus  $K^*$  can be obtained as (Nemat-Nasser et al., 1982; Nemat-Nasser and Taya, 1981; 1985)

$$\frac{K^*}{K} = 1 - \frac{\bar{\epsilon}_{11}^*}{\epsilon_{11}^0} f \quad (1)$$

where  $K$  is the bulk modulus of the matrix material and  $\bar{\epsilon}_{11}^* = \bar{\epsilon}_{22}^* = \bar{\epsilon}_{33}^*$  are the only non zero components of the average transformation strain within the void when the average strain of the material is prescribed to be  $\epsilon_{ij}^0 = \frac{1}{3}\epsilon^0\delta_{ij}$  ( $\delta_{ij}$  being the Kronecker delta).

Similarly, the effective shear modulus  $\mu^*$  can be calculated by considering a unit cell of the material subjected to an average strain whose only non-zero components are  $\epsilon_{12}^0 = \epsilon_{21}^0$ . In this case the only non-zero components of the average transformation strain will be  $\epsilon_{12}^* = \epsilon_{21}^*$ , and the effective shear modulus can be obtained as (Nemat-Nasser et al., 1982; Nemat-Nasser and Taya, 1981; 1985)

$$\frac{\mu^*}{\mu} = 1 - \frac{\bar{\epsilon}_{12}^*}{\epsilon_{12}^0} f \quad (2)$$

where  $\mu$  is shear modulus of the matrix material.

At this point, what remains is the calculation of the average transformation strains  $\bar{\epsilon}_{11}^*$  and  $\bar{\epsilon}_{12}^*$  for the cases of dilatation and shear, respectively. These can be obtained from:

$$\epsilon_{ij}^0 = (A_{ijkl} - S_{ijkl})\bar{\epsilon}_{kl}^* \quad (3)$$

where  $\mathbf{A}$  is a tensor that depends on the elastic mismatch between the two phases (for the more general case of inclusions rather than voids) and  $\mathbf{S}$  is analogous to Eshelby's tensor and maps the transformation strain to the constrained strain. The form of these two tensors is provided in Appendix A.

<sup>6</sup> Note that this arrangement introduces an additional approximation for the Gurtner-Durand architecture, since for this lattice the voids in the numerical model are located on a tetragonal lattice rather than a simple cubic lattice.

### 3.3.2. Truss-lattices with randomly excluded struts

For the case of truss-lattices with randomly excluded struts the selected analytical model is the Mori–Tanaka method (Mori and Tanaka, 1973). This model assumes that a distribution of either random or aligned dilute ellipsoidal inclusions exist in a matrix with a uniform average stress. Since here we limit consideration to the case of an isotropic matrix with spherical voids, the solution of the Mori–Tanaka model coincides exactly with that of the Hashin–Shtrikman upper bound (Weng, 1984) for both the effective bulk and shear moduli, which therefore can be calculated as:

$$K^* = K - f \left( \frac{1}{K} - \frac{3(1-f)}{3K+4\mu} \right)^{-1}, \quad (4)$$

$$\mu^* = \mu - f \left( \frac{1}{\mu} - \frac{6(1-f)(K+2\mu)}{5\mu(3K+4\mu)} \right)^{-1}, \quad (5)$$

## 4. Results

This section provides the numerical, analytical, and experimental findings of our investigation. We first present the results for the cases regarding voids, followed by the results regarding random dispersions of missing struts.

### 4.1. Elastic properties of truss-lattices with voids

For the elastic response of truss-lattice materials with voids, we will investigate the effects of void size first, followed by void volume fraction, and finally the relative position between voids.

#### 4.1.1. Effect of void size

To investigate the effect of void size, we consider the case of uniformly distributed voids at a single void volume fraction. For a homogeneous continuum material, the effect of a void is dependent only on the void volume fraction, with the absolute size of the void having no impact on the modulus reduction. Conversely, for heterogeneous materials such as the discrete truss-lattice materials considered here, the effect of a void that exists near the characteristic length scale of the material is expected to be dependent on the absolute size of the void. It is only when a separation of scales exists between the size of the void and the length scale of the material (i.e. when  $n \gg 1$ ) that the effect of the void will converge to the effect it would have in a homogenized representation of the heterogeneous material. To investigate such scale effects, we fix the number of voids to  $p = 1$  and the void volume fraction to  $f = 0.125$  (so that  $N = 2n$ ), and computed the bulk, shear, and Young's moduli while varying  $n$  between 2 and 15. The results of this investigation are plotted in Fig. 4. The most striking trend from these plots is that for the more highly connected octet and Gurtner–Durand architectures, the effect of the void on the elastic constants is identical for all the values of  $n$  analyzed. An extension of this investigation to  $n = 1$  revealed the same trend for these architectures, even for this case when the size of the void exists as close as possible to the characteristic length scale of the truss-lattice material (given by the axial length of the struts). As such, it can be concluded that the change in elastic constants from the presence of voids for these two architectures is identical to that for homogeneous materials. Remarkably, this is the case for any  $n \geq 1$ , making it clear that this is an intrinsic property of the octet and Gurtner–Durand architectures, independent of any scaling effects. On the other hand, for the architectures with lower coordination numbers (the tetrakaidecahedron and octahedron) the elastic moduli converge in an exponential-like form to that of the equivalent continuum material as  $n$  increases, though at a rate which is different for each architecture and elastic constant. A comparison of the curves for the tetrakaidecahedron and octahedron architectures shows that the bulk and shear moduli span a larger range for the former, while the Young's modulus spans a larger range for the latter. Thus, for architectures that are sensitive to void size effects, there are factors in addition to the coordination number that govern the response to voids.

Overall, these results are consistent with the idea that the effect of  $Z$  decreases as the separation of scales between void size and material length scale increases. That is, as  $n$  grows large, the response to defects depends solely on the elastic constants of the effective medium. It is for this reason that the results for the octahedron approach that for the octet as  $n$  increases, since these two architectures exhibit nearly identical anisotropy (as reported in Table 2). As for the effect of coordination number, it is natural to expect that as  $Z$  tends towards large numbers the discreteness of a truss-lattice material will begin to approximate the complete connection of material present in continuous materials. Surprisingly, our analyses reveal that  $Z$  only needs to be on the order of 12–14 for the effect of voids on the elastic properties of a discrete material to be identical to that of a continuous one.

#### 4.1.2. Effect of void volume fraction

The effect of void volume fraction on the elastic properties of all architectures is shown in Figs. 5a, b and 6a. The numerical results on these plots correspond to a void size  $n = 3^7$  while the supercell size  $N$  is varied between 5 and 10, to

<sup>7</sup> The value  $n = 3$  is selected so that the results correspond to a void size in the scale dependent regime, while offering a more varied set of void volume fractions than can be surveyed by choosing  $n = 1$  or  $n = 2$ .

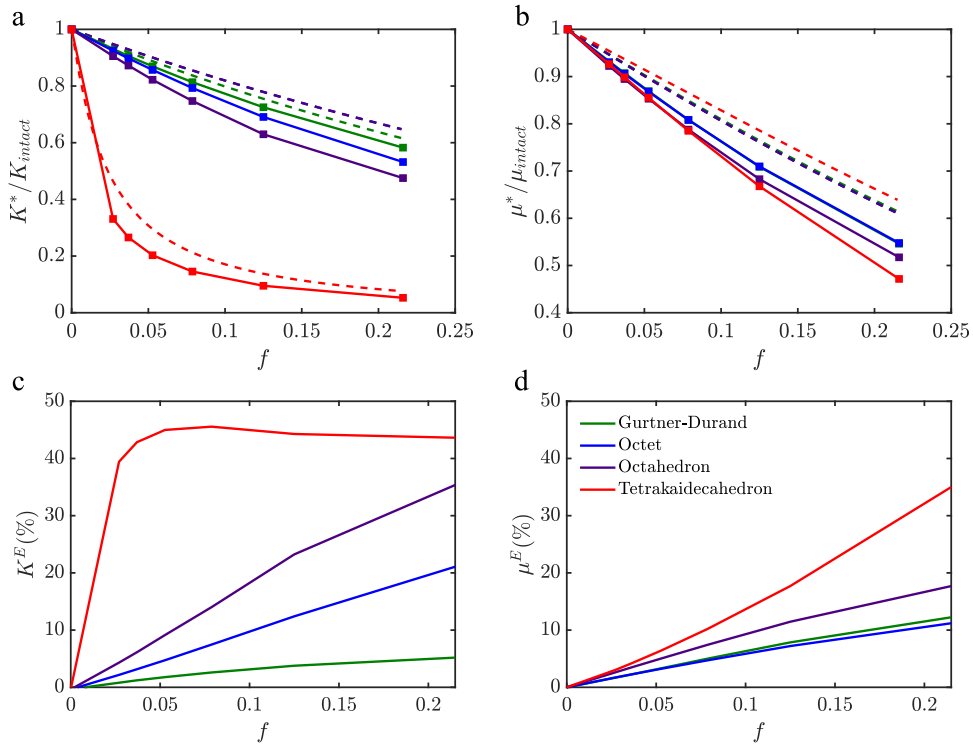


**Fig. 5.** (a-b). Dependence of the (a), bulk modulus and (b), shear modulus on the void volume fraction for a uniform void distribution. Solid lines correspond to the numerical results, and dashed lines to the analytical solution. For architectures where void size effects exist (octahedron and tetrakaidecahedron), the numerical curves correspond to a void size  $n = 3$ . Note that shear modulus curves from the numerical models of the octet and Gurtner-Durand architectures coincide so closely that the curve for the Gurtner-Durand is visually obstructed. Also, the analytical curves for the octahedron and octet coincide so closely for both moduli that the curves for the octet are visually obstructed. (c-d). The percent difference  $(\cdot)^E$  between the numerical and analytical models for (c), bulk modulus and (d), shear modulus for the truss-lattice architectures with uniform void distribution.

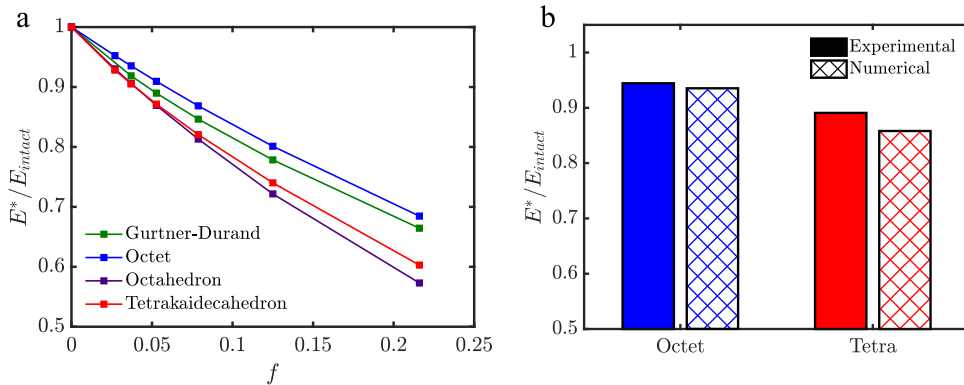


**Fig. 6.** (a). Dependence of the Young's modulus on the void volume fraction for a uniform void distribution. For the octahedron and tetrakaidecahedron topologies, where void size effects exist, the curves correspond to a void size  $n = 3$ . (b). Comparison of the numerical results to the experimental specimens with the void configuration introduced in Fig. 1e.

obtain a range of volume fractions between 0.027-0.216. A pair of curves for the bulk and shear moduli are plotted for all architectures in Fig. 5a and b, where the solid curves correspond to the finite element results and the dashed lines to the values calculated with the analytical model, calculated by using Eqs. (1) and (2). The most apparent trends from the simulations are consistent with the literature on solids containing voids and two-dimensional truss-lattice materials (Guo and Gibson, 1999; Silva and Gibson, 1997; Symons and Fleck, 2008). Namely, the elastic properties degrade with increasing void volume fraction for all materials, and the sensitivity to defects tends to be less for architectures with higher coordination number. Additionally, across most of the range of void volume fraction reported, the ordering of both moduli follow the same sequence observed in Fig. 4 at  $n = 3$ .

The effect of coordination number can be further understood by comparing the numerical curves for the octet and the octahedron shown in Fig. 5a and b. As can be observed in Table 2, the elastic constants for these two architectures are related, with every elastic constant for the octet approximately equal to twice the value for the octahedron. As a result, the two architectures also have nearly identical universal anisotropy indices (Ranganathan and Ostoja-Starzewski, 2008)<sup>8</sup>,  $A^U$ , and the analytical models generate nearly identical curves for the effective moduli of these architectures. The observed difference between the two numerical curves can therefore be fully attributed to the lower coordination number of the octahedron and the associated scale effects for this architecture, triggering a faster rate of degradation among all elastic constants in the presence of uniformly distributed voids. It should also be noted that the coordination number will have an impact only on the numerical results for the tetrakaidecahedron and octahedron architectures, since the octet and Gurtner-Durand have been shown to be free of scale effects (and thus free from dependence on the coordination number) for uniformly distributed voids. Thus, for the octet and Gurtner-Durand, the main discrepancy between the analytical and numerical curves for the octet and Gurtner-Durand architecture can be attributed to anisotropy.

At this point it is important to point out that, although the coordination number is an important parameter, it is not the only difference between the architectures considered. They each have different elastic properties, which must also be considered when interpreting these results.

For example, the rapid reduction of the bulk modulus for the tetrakaidecahedron at small void volume fractions may easily be mistaken to be a result of its low coordination number, however this general behavior is present in the result of the analytical model as well (Fig. 5a). The analytical model is insensitive to the coordination number and assumes a homogeneous material outside the voids, yet it is capable of capturing this sudden drop. This comparison reveals that the source for the precipitous drop in bulk modulus for the tetrakaidecahedron is more a consequence of the effective-material being near the incompressible limit (i.e.  $K \gg \mu$ , as can be calculated from the elastic constants provided in Table 2) than the low coordination of the underlying architecture.

Finally, in Fig. 5c and d we show the percent error of the analytical model, denoted as the modulus with a superscript  $E$  and calculated as  $(\cdot)^E = [((\cdot)_{anal} - (\cdot)_{FEM})/(\cdot)_{FEM}] * 100\%$ , where  $(\cdot)$  is either  $K$  or  $\mu$  for the bulk and shear modulus respectively. These plots provide additional insight on the difference between the results of the numerical and analytical models for the effective bulk and shear moduli. It can be seen that the percent error between the analytical and numerical models is inversely proportional to the coordination number of the truss-lattice architecture. Furthermore, the analytical model error generally increases as the volume fraction  $f$  increases. The rate of this increase is topology dependent, with the bulk modulus of the tetrakaidecahedron being the only outlier from this trend. It is noted that for the highly connected Gurtner-Durand architecture the difference between the analytical and numerical models is relatively small. Even at the largest defect volume fraction considered,  $f = 0.216$ , the analytical model predicts a value for the bulk and shear moduli only 5.5% and 12.3% higher than the numerical calculations, respectively. These observations provide further evidence that truss-lattice materials with sufficiently high coordination numbers can be reasonably described by models developed for classical Cauchy continua.

While in Fig. 5 we compare analytical and numerical predictions for the shear and bulk modulus of the defected architectures as a function of  $f$ , in Fig. 6 we focus on the Young's modulus to compare experimental and numerical results. The dependence of the Young's modulus on the void volume fraction is observed to be similar to the other moduli reported in Fig. 5. Again, the ordering of architectures by modulus is consistent with the sequence observed in Fig. 4 at  $n = 3$  across the range of void volume fraction reported here. Therefore, it can be inferred that void size effects are responsible for the curve of the octahedron lying beneath the tetrakaidecahedron, and that the difference in effective elastic properties are responsible for the curve of the octet lying above the Gurtner-Durand.

For experimental verification of the numerical models with a uniform void distribution, we compare the results of the octet and the tetrakaidecahedron architectures from Section 2 to an additional numerical model with void size  $n = 1$  and supercell size  $N = 3$ , corresponding to a void volume fraction  $f = 0.037$ . Consistent with the results from the void size study, this additional numerical model yields a lower prediction for the modulus of the tetrakaidecahedron than the result reported in Fig. 6a, since the current model uses a smaller void size. The normalized effective modulus calculated from the numerical models is compared to the experimentally measured values in Fig. 6b, where a very satisfactory agreement between the experimental and numerical findings for both architectures can be observed. Potential sources of discrepancy are the compliance of the load frame, the finite size of the fabricated specimens, the increased flexural stiffness of the composite beams in the experiment, variation in properties of the polymer, and geometric defects (e.g. nodal position) of the polymer template. Nonetheless, the agreement between the numerical models and experimental results provides verification of the approach used for the numerical models. Furthermore, it is demonstrated that the effect of defects in experimental specimens with nanoscale feature sizes can be accurately captured with scale independent models of beam networks.

<sup>8</sup> The anisotropic index  $A^U$  is defined as

$$A^U = 5 \frac{\mu^V}{\mu^R} + \frac{K^V}{K^R} - 6$$

where  $\mu^V$  and  $\mu^R$  are the Voigt and Reuss estimates for the shear modulus and  $K^V$  and  $K^R$  are the Voigt and Reuss estimates for the bulk modulus. This index takes a minimum value of 0 for isotropic materials, with an increasing value for the index indicating further departure from isotropy.

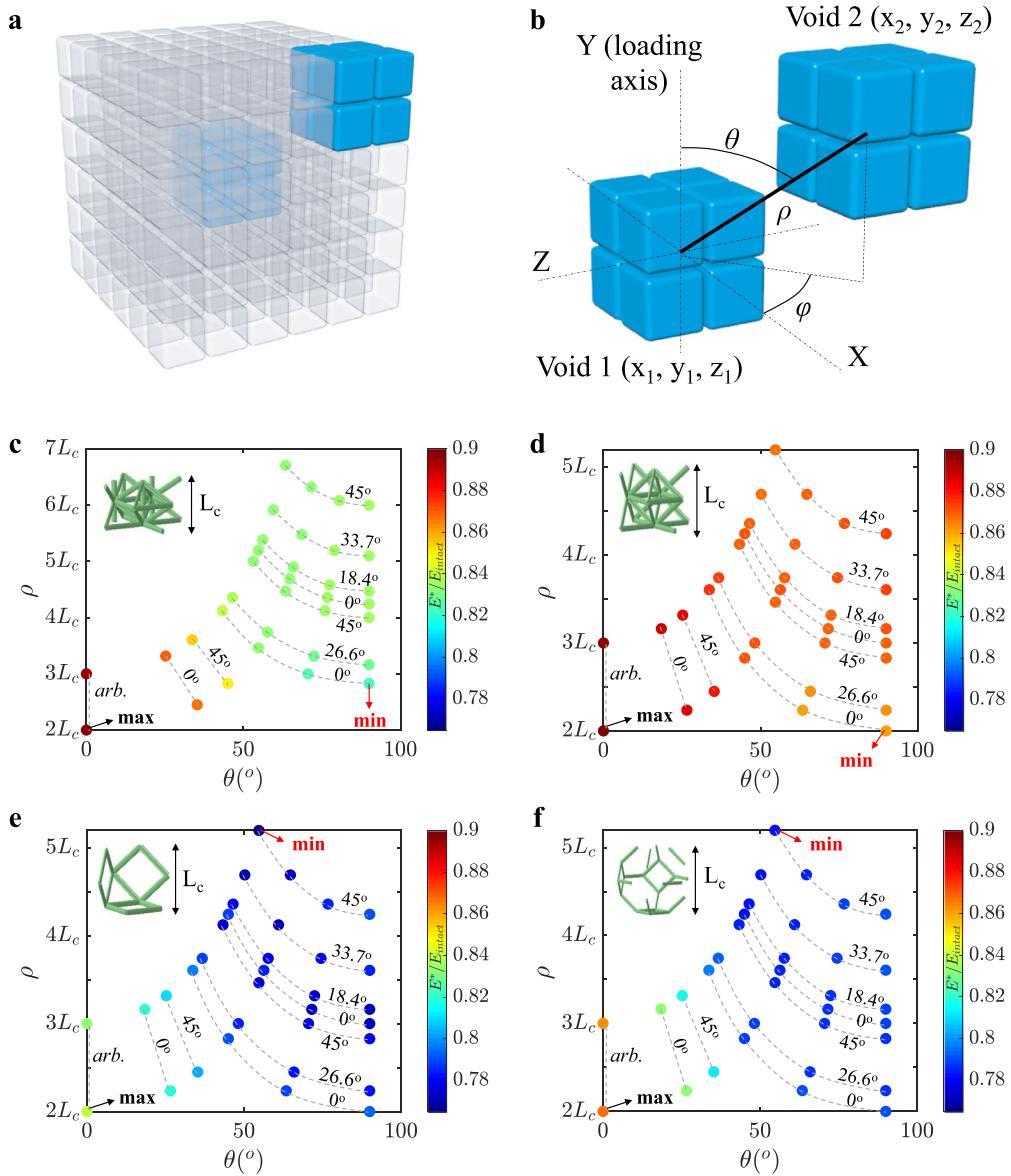


**Fig. 7.** (a). Schematic view of a non-uniform void distribution with two  $2 \times 2 \times 2$  voids in a  $6 \times 6 \times 6$  supercell ( $p = 2, n = 2, N = 6$ ). (b). Definition of the spherical coordinate system. One void is fixed at the center of the supercell and the other is placed in all possible locations.  $\rho$  is the distance between the voids,  $\theta$  is the zenith angle and  $\phi$  is the azimuth angle. (c-f). The dependence of the effective Young's modulus (normalized by the intact Young's modulus) on the relative position between the voids for all architectures. The color of each point corresponds to the effective Young's modulus and dashed lines connect neighboring points that have equal azimuth angle  $\phi$ , with the value given beside each line. The cases corresponding to the maximum and minimum effective modulus are also indicated. (For interpretation of the references to color in this figure legend, the reader is referred to the web version of this article.)

#### 4.1.3. Effect of void relative positioning

Although the analysis of uniformly distributed voids is critical to understand the fundamental behavior of the different architectures to voids, in most self-assembled materials the void population will be disordered, motivating the investigation of non-uniform void distributions. To this end, we start by seeking Young's modulus for a supercell with  $N = 6$  that contains two voids ( $p = 2$ ) each of size  $n = 2$  (resulting in  $f = 2/27 \approx 0.0741$ ). The first void is arbitrarily fixed at the center of the supercell, while, taking advantage of symmetry in the relative void position and loading (uniaxial stress in the Y-direction), the second void is placed in one of the 34 available positions in a sixteenth of the supercell (Fig. 7a) and its position is fully identified by  $\rho, \theta$  and  $\phi$ .  $\rho$  is the distance between the voids centers,  $\theta$  is the zenith angle and  $\phi$  is the azimuth angle (Fig. 7b). The numerical results reveal that the Young's modulus in the loading direction is relatively insensitive to the azimuthal coordinate,  $\phi$ , allowing for the presentation of the reduced modulus results with respect to only the radial and

**Table 3**

Statistical properties of the Young's modulus variation with non-uniform distribution of voids. The column labeled "UDV" corresponds to the results for uniformly distributed voids, and its values are interpolated from the trends of Fig. 6.

Architecture	Min	Max	Mean	Std. Dev.	UDV
Tetraikadehedron	0.7822	0.8670	0.7965	$21.58 \times 10^{-3}$	0.8125
Octahedron	0.7654	0.8393	0.7883	$17.99 \times 10^{-3}$	0.7983
Octet	0.8600	0.9024	0.8730	$9.328 \times 10^{-3}$	0.8765
Gurtner-Durand	0.8268	0.8971	0.8361	$16.83 \times 10^{-3}$	0.8557

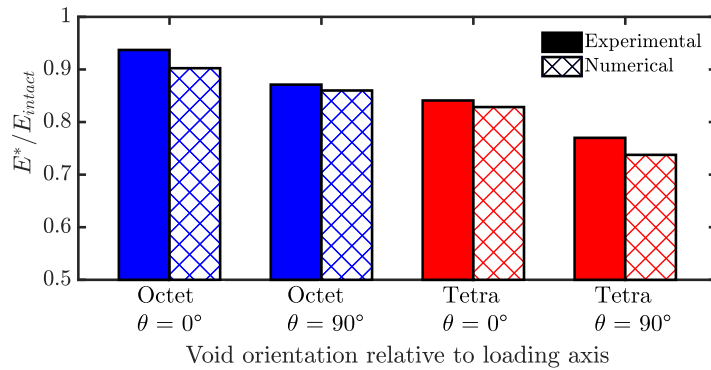


**Fig. 8.** Experimental verification of the non-uniform void distribution analysis, plotting the normalized Young's modulus against two voided cases for the octet and the tetraikadehedron architectures. The void size is two unit cells ( $n = 1$ ,  $N = 3$ ,  $p = 2$ , resulting in  $f = 0.074$ ), with the elongated side of the void placed either parallel ( $\rho = 2L_C$  and  $\theta = 0^\circ$ ) or normal ( $\rho = 2L_C$  and  $\theta = 90^\circ$ ) to the loading axis.

zenith spherical coordinates, as shown in Fig. 7c–f. The data indicate that the most favorable position for the two voids is the same for every architecture, corresponding to the case of adjoining voids with the long direction of the adjoined void aligned to the loading direction. The most unfavorable position for the two voids is found to be architecture dependent. Simple statistical measures of these results are summarized in Table 3, which also includes the interpolated value of the modulus if a configuration of uniformly distributed voids existed at the same defect volume fraction. The table indicates that the uniform void distribution always has a slightly less deleterious effect on the modulus than the mean of all the non-uniform spacing cases, and tends to be near the center of the range of results for non-uniform void spacing. Given the mean and range for the non-uniform void spacing, it is clear that modulus reduction is dominated by void volume fraction, although the effect of non-uniform spacing is non-negligible. The importance of void volume fraction over void placement is further examined by calculating the reduction in bulk modulus for the three void arrangements associated with extremal values in Fig. 7c–f for all architectures. The results for bulk modulus are consistent with those for Young's in these extremal cases, further supporting the conclusion that the effect of void volume fraction dominates void arrangement. With this finding firmly supported, exhaustive analysis of void placement for the bulk modulus and calculation of shear modulus reduction are forgone.

Experimental verification of the numerical models with non-uniform void distributions is conducted through examination of tetraikadehedron and octet specimens that are  $3 \times 3 \times 3$  tessellations of a supercell like the one depicted in Fig. 1d, but with one additional unit cell removed adjacent to the central one to form an elongated void. Two orientations of this elongated void are considered for each architecture, in the first the elongated dimension of the void is aligned with the loading axis, and in the second it is perpendicular to the loading axis. The former orientation corresponds to the most favorable void positioning for both architectures ( $\rho = 2L_C$  and  $\theta = 0^\circ$ , where  $L_C$  is the length of the unit cell as defined in Fig. 7 for each architecture), while the latter configuration is the most unfavorable for the octet topology ( $\rho = 2L_C$  and  $\theta = 90^\circ$ ). The volume fraction in both cases is  $f = 0.074$ . The experimental values are compared to the numerical models of a  $3 \times 3 \times 3$  supercell with the same void arrangement and periodic boundary conditions. The results of this investigation are reported in Fig. 8. It can be seen that the experimentally measured values for all void arrangements lie within a few percent of the predicted values from the numerical models, with the numerical models consistently indicating a slightly lower estimation of the normalized Young's modulus. The general agreement between simulation and experiment supports the conclusion that the normalized modulus reduction is more sensitive to the void volume fraction than the relative void positioning, though the impact of the latter is confirmed to be non-negligible.

#### 4.2. Elastic properties of lattices with random defects

With the perspectives gained from investigating defects in the form of voids, which exhibit an underlying order, we now turn to disordered defects by investigating the response of the truss-lattice architectures when some of their struts

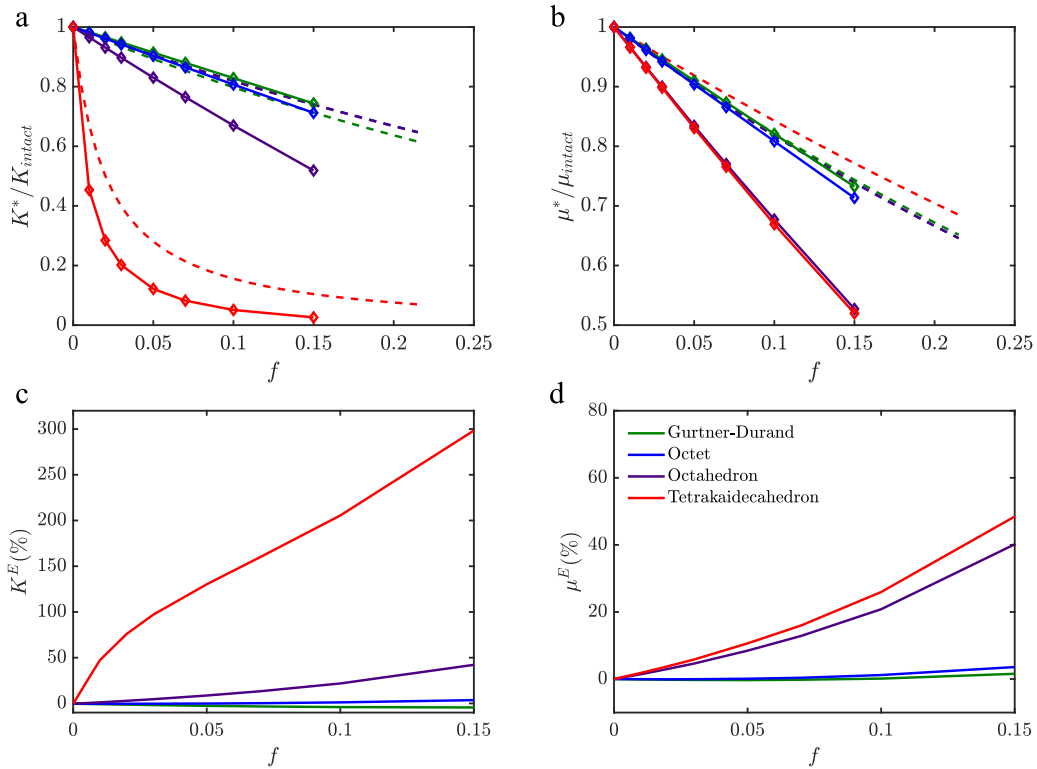


**Fig. 9.** (a-b). Dependence of the (a). bulk modulus and (b). shear modulus on the volume fraction of randomly excluded struts. Solid lines correspond to the numerical results, and dashed lines to the analytical solution. The analytical curves for the octahedron and octet coincide so closely for both moduli that the curves for the octet are visually obstructed. (c-d). The percent difference ( $\cdot$ )<sup>E</sup> between the numerical and analytical models for (c). bulk modulus and (d). shear modulus for the truss-lattice architectures with randomly excluded struts.

**Table 4**

Slope of the best fit lines to the data from the numerical models reported in Figs. 9a, b and 10a. Absolute value of the slope is reported. The values indicate the rate of reduction in the elastic property per volume fraction of randomly excluded struts.

Architecture	$K$	$\mu$	$E$
Tetrakaidecahedron	non-linear	3.22	4.06
Octahedron	3.22	3.16	3.11
Octet	1.92	1.91	1.89
Gurtner-Durand	1.71	1.78	1.59

are randomly excluded. The effect of different volume fractions of randomly excluded struts on the elastic properties of the truss-lattice architectures is shown in Fig. 9a and b (bulk and shear) and Fig. 10a (Young’s). In these plots the data markers correspond to the mean values from the sets of 1000 simulations performed for each volume fraction of randomly excluded struts in an 8x8x8 periodic supercell, while the dashed lines correspond to the results from the analytical model, calculated by using Eqs. (4) and (5). The most apparent trend from the numerical results is that the rate of elastic property degradation with increasing void volume fraction is inversely proportional to the coordination number. This trajectory is particularly clear with regards to the Young’s modulus, though it is also present in the bulk and shear modulus plots. With the exception of the bulk modulus for the tetrakaidecahedron, the relationships between the effective moduli and void volume fraction are nearly linear across the range of defect volume fraction investigated. As a result, these relationships can be characterized by the slope of the best fit line, which is a dimensionless number that physically corresponds to the rate of reduction in the elastic property per volume fraction of randomly excluded struts. The absolute value of these slopes for each architecture and modulus are reported in Table 4. It is observed that for all of the architectures, other than the tetrakaidecahedron, the degradation rates are nearly identical across the three moduli. This consistency points toward the effect of coordination number. However, just as in the case of voids, the elastic properties of the effective-material must also be considered when analyzing the results. Indeed, it is again the nearly incompressible behavior of the tetrakaidecahedron

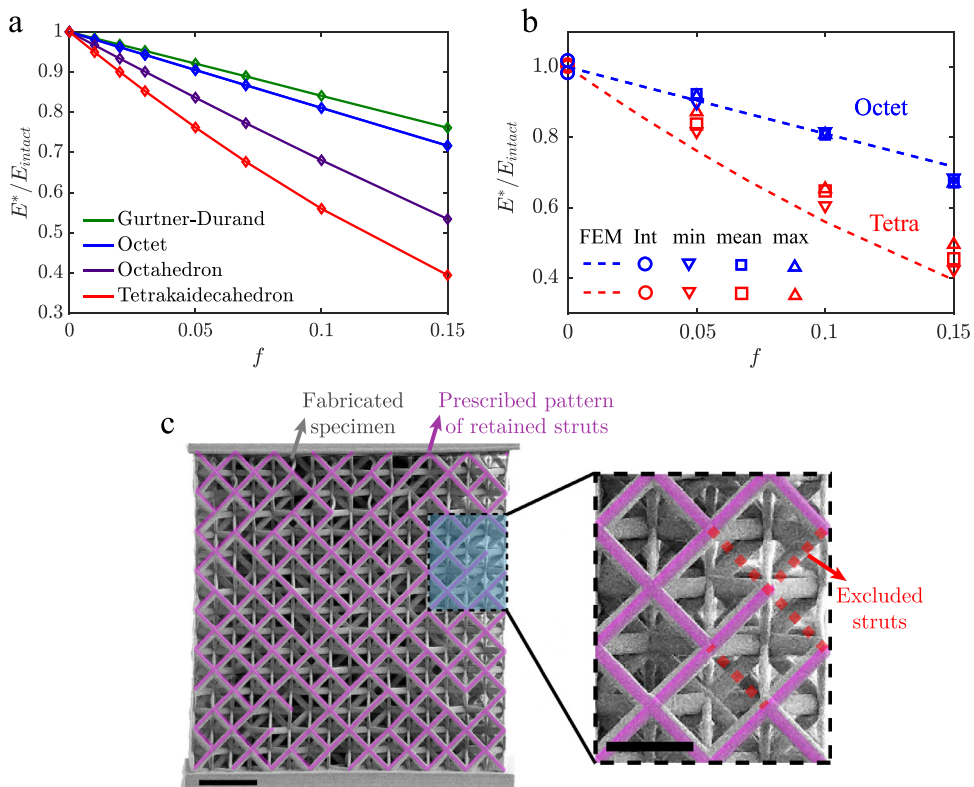


**Fig. 10.** (a). Dependence of the Young's modulus on the volume fraction of randomly excluded struts for all architectures. A clear trend between the coordination number and the slopes of the decreasing trends can be observed. (b). Experimental data (markers) and numerical results (dashed lines) for the effective Young's modulus at different volume fractions of randomly excluded struts for the octet and tetrakaidecahedron architectures. The experimental specimens correspond to the defect realizations in the numerical study which experienced the minimum, mean, and maximum reduced modulus. (c). SEM image of an  $8 \times 8 \times 8$  octet specimen with randomly excluded struts ( $f = 0.15$ ). An overlay of the struts on the exterior face for the prescribed defect realization is in fuchsia. 10  $\mu\text{m}$  scale bar. Inset image also indicates intentionally excluded struts in red (5  $\mu\text{m}$  scale bar). (For interpretation of the references to color in this figure legend, the reader is referred to the web version of this article.)

that greatly contributes to the increased sensitivity of its bulk modulus to random strut exclusions, as captured in the analytical model.

Further comparison between the analytical models and numerical results are instrumental in assessing the different contributions to the modulus reduction. Fig. 9c and d shows the relative error in the effective moduli between the analytical models and numerical results. To better understand the sources of the discrepancy between numerical and analytical curves, we start by comparing the response of the octet and Gurtner-Durand, which both have large coordination numbers, but significantly different levels of anisotropy. Since the error of the analytical model is quite low for both architectures, we can infer that the discrepancy is not extremely sensitive to anisotropy. Second, we compare the results for the octahedron and octet architectures. These two truss-lattice materials have nearly identical levels of anisotropy, but the octahedron has a lower coordination number. The error of the analytical model is substantially larger for the octahedron architecture, suggesting that the effect of coordination number dominates the error. These observations provide the strongest evidence yet that truss-lattice materials with lower coordination numbers are the most sensitive to randomly excluded struts. This remains true even when the effective elastic properties of the pristine material ensure a high sensitivity to defects, as in the case of the bulk modulus of the tetrakaidecahedron. Moreover, the excellent agreement between the analytical models and the numerical results for the octet and Gurtner-Durand architectures suggests that the critical observation from the preceding section on voids can be extended to the case of randomly excluded struts. That is, for highly connected truss lattices (at least in the range of 12 – 14), the dependence of the elastic properties on random defects can be identical to that for continuous materials.

Truss-lattices with randomly dispersed defects were also experimentally tested for the tetrakaidecahedron and octet architectures. Three realizations of random defects were tested at defect volume fractions of  $f = 0.05, 0.1, 0.15$  on specimens with a tessellation size of  $8 \times 8 \times 8$ . The defect realizations were chosen from the set of 1000 realizations used in the numerical simulations performed for each architecture at each level of defect volume fraction, as described in Section 3.2. At each defect volume fraction the selected realizations for the experimental specimens were the ones that caused the minimum, mean, and maximum reduction in stiffness from the ensemble of 1000 realizations. Fig. 10c shows a gray-scale SEM

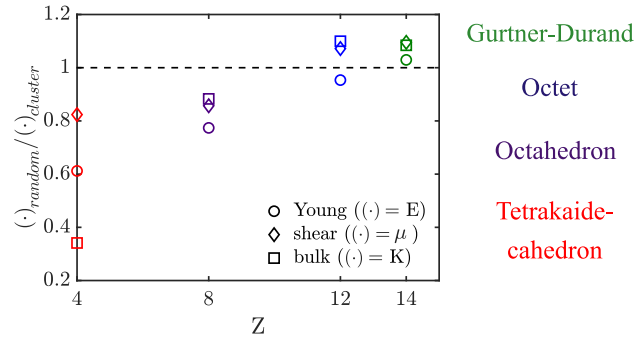


**Fig. 11.** Comparison between the effect of randomly excluded struts and uniformly distributed voids on the moduli for all architectures. The ratio of effective modulus with random defects to the effective modulus with voids is shown across the range of coordination numbers at a defect volume fraction  $f = 0.125$ . As  $Z$  increases, the random removal of struts has a less deleterious effect than the uniform void distribution, across all topologies and moduli. The values for the effective moduli with random defects are linearly interpolated from the results at  $f = 0.1$  and  $f = 0.15$ . The values for the effective moduli with a uniform void distribution have been calculated for a void size  $n = 15$ , where void size effects are minimized for the tetrakaidecahedron and octahedron architectures.

image of the octet experimental specimen with the defect realization that causes the mean reduction in stiffness at a defect volume fraction  $f = 0.15$ . Overlaid on the experimental image in fuchsia is an image from the numerical model that shows the struts on the exterior surface for this particular realization of defects. It can be observed from the composite image that the intended defect realization is well captured in the experimental specimen.

The experimental results are plotted in Fig. 10b with marker points, along with the Young's modulus from the numerical models of these two architectures (dashed lines). It is apparent that the measurements of the reduction in Young's modulus with defect volume fraction from the experiments are in excellent agreement with the numerical results. Furthermore, no correlation exists between the defect realization and modulus reduction for the octet specimens, with the effect of the specifically selected defect realizations from the numerical study being outweighed by experimental scatter. This realization insensitivity provides strong evidence that sufficiently large experimental specimens have been tested to measure a material property, rather than a property of the particular defect realizations used in the specimens tested. As a result of both the realization insensitivity and correspondence to simulation results, the behavior of the octet architecture is experimentally confirmed to respond to the presence of random defects in a manner that is identical to a continuous material, at least for defect volume fractions up to  $f = 0.15$ . For the tetrakaidecahedron specimens, a stronger correlation between the particular defect realization and the elastic modulus exists, so that at each defect volume fraction, the order of the stiffnesses in the experiments matched those in the simulations. Even with this larger dependency on the specific defect realizations, close matching was found between the average experimental response and the numerical results for the tetrakaidecahedron architecture. Results that are independent of the specific defect realization chosen for each tetrakaidecahedron specimen would require larger tessellations and were not pursued due to the fabrication time that would be required and the satisfactory agreement of the current results between simulation and experiment.

## 5. Discussion and conclusions

Further understanding regarding the behavior of imperfect truss-lattice materials can be achieved by comparing the effect that the different defect distributions considered (voids vs. random) have on the elastic properties. Although the degradation of elastic properties is always dominated by the defect volume fraction, it is found that the least deleterious type of defect is architecture dependent. In other words, for some architectures it is more favorable to have voids than randomly excluded struts and vice versa. Fig. 11 is illustrative of this behavior, where the ratio of the effective modulus for random removal to that for uniform voids for each of the three moduli is plotted against the coordination number at a defect volume fraction of  $f = 0.125$ . The data clearly reveal that as the coordination number increases, the random removal of struts becomes more preferential than the uniform void distribution. This trend is apparent across all architectures and moduli, with the Gurtner-Durand being the only architecture investigated for which random strut removal is actually less detrimental than the uniform void arrangement for all elastic moduli. It is left as an open question whether this preference for random strut removal could be indicative that sufficient redundancy exists within the truss-lattice so that architectures with higher coordination numbers will stop returning improved properties. Further investigation would be necessary to answer this question as well as consider if the correlations found between coordination number and elastic properties are sensitive to effects other than topology (e.g. junction angle between struts, symmetries, etc.), as we only consider one truss-lattice architecture for each coordination number. Nonetheless, within the scope of this study the correlation between elastic properties and topology is strong.

To summarize, this investigation on the elastic response of truss-lattice materials to defects has both quantified the effective elastic properties for these materials when defects are present and revealed a new characteristic of imperfect truss-lattices. It has been found that the change in elastic properties of highly connected truss-lattice materials ( $Z \geq 12$ ) to the

presence of defects is indistinguishable from that of a homogeneous material. This phenomenon is directly observed when defects take the form of voids, due to the absence of scale effects. When the defects take the form of randomly excluded struts, correspondence of the response for the highly connected truss-lattice materials to the Mori–Tanaka model demonstrates that this phenomenon remains unchanged. Accordingly, for these highly connected truss-lattice materials, models developed for classical Cauchy continua can accurately be applied to describe their effective properties in the presence of defects. Truss-lattice materials with lower coordination numbers do not exhibit this remarkable property, and for analytical models to accurately describe their properties they must consider additional information, such as the coordination number. Even after accounting for differences in effective elastic properties, less-connected truss-lattice materials are found to be more sensitive to defects than their more-connected counterparts. Furthermore, the most favorable arrangement of defects is also found to be correlated to coordination number, with less degradation of elastic properties occurring for the case of random defects in more-connected truss-lattice than for the case of voids, and vice versa for less-connected truss-lattices. Finally, we want to emphasize that although in all numerical analyses we considered struts to have an elliptical cross-section with major to minor axis dimensions of 2:1 and strut aspect ratio  $\lambda = 19.17$ , the strut geometry does not directly influence the response of the material to the presence of defects. Additional analyses presented in [Appendix C](#) show that the geometry of the struts in a truss-lattice only influence its response to the presence of defects indirectly by means of modifications to its elastic properties.

### Acknowledgements

This work was supported in part by [Charles Stark Draper Laboratory](#) with funding and access to in situ mechanical testing equipment. We appreciate motivating discussions with David Carter and the lab assistance provided by Ernie Kim. The fabrication was performed at Harvard University's Center for Nanoscale Systems (CNS), a member of the National Nanotechnology Coordinated Infrastructure (NNCI), which is supported by the [National Science Foundation](#) under NSF award no. 1541959.

### Appendix A. Form of the tensors $\mathbf{A}$ and $\mathbf{S}$ entering in Eq. (3)

To derive explicit expressions for the tensors  $\mathbf{A}$  and  $\mathbf{S}$  entering in [Eq. \(3\)](#), we focus on an elastic matrix with elastic constants  $C_{ijkl}$  and a simple cubic periodic distribution of elastic inclusions with elastic constants  $\bar{C}_{ijkl}$ . For such a system we seek the transformation strain  $\epsilon^*$  in the domain of the inclusions  $\Omega$  that satisfies the following expression ([Nemat-Nasser et al., 1982; Nemat-Nasser and Taya, 1981; 1985](#)):

$$C_{ijkl}(\epsilon_{kl}^0 + \epsilon_{kl} - \epsilon_{kl}^*) = \bar{C}_{ijkl}(\epsilon_{kl}^0 + \epsilon_{kl}) \quad \text{in } \Omega \quad (\text{A.1})$$

where  $\epsilon^0$  and  $\epsilon$  are the average and periodic strains in a unit cell, respectively.

First, we rewrite [Eq. \(A.1\)](#) as:

$$\epsilon_{ij}^0 = A_{ijkl}\epsilon_{kl}^* - \epsilon_{ij} \quad \text{in } \Omega \quad (\text{A.2})$$

with

$$A_{ijkl} = (C_{ijmn} - \bar{C}_{ijmn})^{-1} C_{mnlk} \quad (\text{A.3})$$

As shown in [Nemat-Nasser and Taya \(1981, 1985\)](#) and [Nemat-Nasser et al. \(1982\)](#), for the case considered here, where the inclusions are voids,  $\mathbf{A}$  reduces to:

$$A_{ijkl} = \frac{\delta_{ik}\delta_{jl} + \delta_{il}\delta_{jk}}{2}, \quad (\text{A.4})$$

$\delta_{ij}$  being the Kronecker delta.

[Eq. \(A.1\)](#) also allows the total stress  $\sigma^T$  in the inclusions to be related to the strains as:

$$\sigma_{ij}^T = C_{ijkl}(\epsilon_{kl}^0 + \epsilon_{kl} - \epsilon_{kl}^*) \quad \text{in } \Omega \quad (\text{A.5})$$

Substituting [Eq. \(A.5\)](#) into the equilibrium condition  $\sigma_{ij,j}^T = 0$ , yields the following relation between  $\epsilon$  and  $\epsilon^*$ :

$$[C_{ijkl}(\epsilon_{kl} - \epsilon_{kl}^*)]_{,j} = 0 \quad \text{in } \Omega \quad (\text{A.6})$$

Next, taking advantage of the periodicity of the system, we express any field quantity  $\alpha(\mathbf{x})$ , as Fourier series ([Nemat-Nasser et al., 1982; Nemat-Nasser and Taya, 1981; 1985](#))

$$\alpha(\mathbf{x}) = \sum_{\mathbf{n}=0}^{\pm\infty} \hat{\alpha}(\boldsymbol{\xi}) e^{i\boldsymbol{\xi}\cdot\mathbf{x}} \quad (\text{A.7})$$

with

$$\xi_j = \frac{2\pi n_j}{\Lambda} \quad (\text{A.8})$$

where  $i$  is the imaginary unit and  $\Lambda = (4\pi R^3/3f)^{1/3}$  is the lattice constant defined by the cubic pattern of voids ( $R$  being the radius of the voids and  $f$  denoting the volume fraction occupied by the voids). Note that this is a three-dimensional Fourier series, so that the terms  $\mathbf{x}$ ,  $\xi$ , and  $\mathbf{n}$  are vector quantities. Substitution of the Fourier series representations with the form given in Eq. (A.7) into Eqs. (A.2) and (A.6), using “the simplest approximation” for the Fourier transformation given, and integration over the domain of the void  $\Omega$ , yields (Nemat-Nasser et al., 1982; Nemat-Nasser and Taya, 1981; 1985):

$$\epsilon_{jl}^0 = \left[ A_{jlmn} - \frac{1}{V} \sum_{\mathbf{n}=\mathbf{0}}^{\pm\infty} g_{jlmn}(\xi) \frac{1}{V_\Omega} \int_\Omega e^{i\xi \cdot \mathbf{x}} d\mathbf{x} \int_\Omega e^{-i\xi \cdot \mathbf{x}} d\mathbf{x} \right] \bar{\epsilon}_{mn}^* \tag{A.9}$$

where  $V = \Lambda^3$  is the volume of the unit cell,  $V_\Omega = 4\pi R^3/3$  is the volume of the void, and the prime on the sum indicates that terms where  $\sqrt{n_k n_k} = 0$  are excluded from summation. Finally, by comparing Eq. (A.9) with Eq. (3) we find that

$$S_{ijkl} = S_{ijkl}^{(1)} - \frac{1}{1-\nu} S_{ijkl}^{(2)} + \frac{\nu}{1-\nu} S_{ijkl}^{(3)} \tag{A.10}$$

where  $\nu$  is the Poisson’s ratio of the matrix material and

$$S_{ijkl}^{(\alpha)} = \sum_{\mathbf{n}=\mathbf{0}}^{\pm\infty} P(\xi) g_{ijkl}^{(\alpha)}(\xi), \quad \alpha = 1, 2, 3 \tag{A.11}$$

with

$$P(\xi) = \frac{9f[\sin(\xi R) - \xi R \cos(\xi R)]^2}{(\xi R)^6}, \quad \text{with } \xi R = 2\pi \sqrt{n_k n_k} \left( \frac{3f}{4\pi} \right)^{1/3} \tag{A.12}$$

$$g_{ijkl}^{(1)}(\xi) = \frac{1}{2} [\bar{\xi}_j (\delta_{il} \bar{\xi}_k + \delta_{ik} \bar{\xi}_l) + \bar{\xi}_i (\delta_{jl} \bar{\xi}_k + \delta_{jk} \bar{\xi}_l)] \tag{A.13}$$

$$g_{ijkl}^{(2)}(\xi) = \bar{\xi}_i \bar{\xi}_j \bar{\xi}_k \bar{\xi}_l \tag{A.14}$$

$$g_{ijkl}^{(3)}(\xi) = \bar{\xi}_i \bar{\xi}_j \delta_{kl} \tag{A.15}$$

and

$$\bar{\xi}_i = \frac{n_i}{\sqrt{n_k n_k}} \tag{A.16}$$

While Eq. (A.10) is general and can be applied to any loading condition, for the case of dilatational and shear deformation considered in this study it reduces to

$$\frac{\bar{\epsilon}^*}{\epsilon^0} = \frac{1}{1 - S_{1111} - 2S_{1122}} \tag{A.17}$$

and

$$\frac{\bar{\epsilon}_{12}^*}{\epsilon_{12}^0} = \frac{1}{1 - 2S_{1212}} \tag{A.18}$$

respectively, with

$$S_{1111} = -\frac{1}{1-\nu} \sum_{\mathbf{n}=\mathbf{0}}^{\pm\infty} P(\xi) (\bar{\xi}_1)^4 + \frac{2-\nu}{1-\nu} \sum_{\mathbf{n}=\mathbf{0}}^{\pm\infty} P(\xi) (\bar{\xi}_1)^2 \tag{A.19}$$

$$S_{1122} = -\frac{1}{1-\nu} \sum_{\mathbf{n}=\mathbf{0}}^{\pm\infty} P(\xi) (\bar{\xi}_1 \bar{\xi}_2)^2 + \frac{\nu}{1-\nu} \sum_{\mathbf{n}=\mathbf{0}}^{\pm\infty} P(\xi) (\bar{\xi}_1)^2 \tag{A.20}$$

$$S_{1212} = \sum_{\mathbf{n}=\mathbf{0}}^{\pm\infty} P(\xi) (\bar{\xi}_1)^2 - \frac{1}{1-\nu} \sum_{\mathbf{n}=\mathbf{0}}^{\pm\infty} P(\xi) (\bar{\xi}_1 \bar{\xi}_2)^2 \tag{A.21}$$

For the numerical implementation of Eqs. (A.19)–(A.21) it was found that truncating the series for wavelengths more than 200 times shorter than the lattice constant provided satisfactory convergence.

**Table B1**

Elastic properties of the tetrakaidecahedron architecture when it is comprised of struts that have circular and elliptical cross-sections. The values in the “Circular” and “Elliptical” columns are calculated from numerical models. The analytical results are calculated using the model developed in [Zhu et al. \(1997\)](#) with geometry that is identical to the numerical model with circular cross-section struts.

Constant	Analytical	Circular	Elliptical
$C_{1111}$	2.06	2.06	2.06
$C_{2222}$	2.06	2.06	2.10
$C_{1122}$	1.99	1.99	1.97
$C_{1133}$	1.99	1.99	2.01
$C_{1212}$	0.0325	0.0320	0.0317
$C_{3131}$	0.0325	0.0320	0.0172
$A^U$	$1.33 \times 10^{-4}$	$1.58 \times 10^{-4}$	0.988

**Table B2**

Elastic properties of the octahedron architecture when it is comprised of struts that have circular and elliptical cross-sections. The values are calculated from numerical models.

Constant	Circular	Elliptical
$C_{1111}$	12.2	12.3
$C_{2222}$	12.2	12.4
$C_{1122}$	5.98	5.91
$C_{1133}$	5.98	6.00
$C_{1212}$	6.08	6.09
$C_{3131}$	6.08	6.07
$A^U$	0.555	0.524

**Table B3**

Elastic properties of the octet architecture when it is comprised of struts that have circular and elliptical cross-sections. The values in the “Circular” and “Elliptical” columns are calculated from numerical models. The analytical results are calculated using the model developed in [Deshpande et al. \(2001\)](#) with geometry that is identical to the numerical model with circular cross-section struts.

Constant	Analytical	Circular	Elliptical
$C_{1111}$	24.2	24.5	24.5
$C_{2222}$	24.2	24.5	24.7
$C_{1122}$	12.1	11.9	11.8
$C_{1133}$	12.1	11.9	12.0
$C_{1212}$	12.1	12.2	12.3
$C_{3131}$	12.1	12.2	12.2
$A^U$	0.600	0.558	0.531

**Table B4**

Elastic properties of the Gurtner–Durand architecture when it is comprised of struts that have circular and elliptical cross-sections. The values are calculated from numerical models.

Constant	Circular	Elliptical
$C_{1111}$	37.9	37.9
$C_{2222}$	39.4	39.7
$C_{1122}$	11.8	11.7
$C_{1133}$	13.4	13.4
$C_{1212}$	12.2	12.2
$C_{3131}$	13.8	13.7
$A^U$	0.0171	0.0180

## Appendix B. Effect of strut geometry on the elastic properties of truss-lattice materials

The effect of strut cross-sectional geometry on the elastic properties of the truss-lattice architectures investigated in this article is provided in Tables B1–B4. All of these values are calculated using a parent material that has an elastic modulus of 2000, a Poisson's ratio of 0.3, and with struts that have an aspect ratio  $\lambda = 19.17$ . The geometry of struts with an elliptical cross-section are identical to those in the main text, as described in Section 3.1. Additionally, the numerical models used to calculate the elastic constants are identical to those in the main text, as described in Section 3.2. For elastic constants excluded in the tables, the following equalities exist:  $C_{3333} = C_{1111}$ ,  $C_{2233} = C_{1122}$ , and  $C_{2323} = C_{1212}$ , except for the Gurtner–Durand with elliptical struts, where  $C_{2323} = 12.3$  as a result of the orientation chosen for the elliptical cross-section on struts that are parallel to the  $y$ -direction. The universal anisotropy index,  $A^U$ , is provided as well. Finally, the results from analytical models for the tetrakaidecahedron and octet architectures, Zhu et al. (1997) and Deshpande et al. (2001) are included to demonstrate the validity of our numerical approach to calculate the elastic properties of bending and stretching dominated truss-lattice materials. The results of the analytical models show excellent agreement with the numerical results when struts have a circular cross-section.

From the data reported here, it is found that the tetrakaidecahedron architecture exhibits elastic properties that are highly dependent on the cross-sectional geometry of the struts, while all other architectures show a much smaller dependence. For example, the Young's modulus (as calculated from the elastic constants provided in Table B1) in the  $y$ -direction for the tetrakaidecahedron increases by 81% when the cross-section is modified from circular to elliptical. Across all architectures, the next largest change found for this material property is substantially smaller at 3.1% for the octahedron. Similarly, the tetrakaidecahedron is the only architecture that exhibits an extreme change in anisotropy from changes to the strut cross-sectional geometry. It is anticipated that the elastic properties of bending dominated truss-lattices, like the tetrakaidecahedron and the octahedron, are the most sensitive to strut cross-sectional shape, but as seen here, extremely different sensitivities can exist across different bending dominated architectures.

## Appendix C. Effect of strut geometry on the mechanical response of imperfect truss-lattice materials

In this Appendix we investigate the effect of (i) cross-sectional geometry, and (ii) strut aspect ratio  $\lambda$  on the Young's modulus of imperfect truss-lattice materials with randomly excluded struts.

### C1. Effect of strut cross-sectional geometry

To investigate the effect of strut cross-sectional geometry, we take the struts to have elliptical cross-sections and vary both the aspect ratio of the ellipse and its orientation with respect to the loading, while maintaining the strut aspect ratio at  $\lambda = 19.17$ . The dependence of the Young's modulus on the volume fraction of randomly excluded struts is shown in Fig. C1. These curves indicate that the tetrakaidecahedron is the only architecture that exhibits a notable sensitivity to the variation in strut cross-sectional geometry, while the other three architectures remain relatively insensitive to this geometric modification. To understand why the tetrakaidecahedron architecture exhibits sensitivity to the cross-sectional geometry, we examine the universal anisotropy index  $A^U$  and the elastic modulus in the loading direction for each geometric variation of every pristine architecture investigated in Fig. C1. In agreement with the results presented in Appendix B, the results reported in Table C1 show that the anisotropy index  $A^U$  is significantly more sensitive to the cross-sectional geometry for the tetrakaidecahedron architecture than any other architecture. Since the dependence of the elastic constants on the volume fraction of randomly excluded struts has been shown to be highly sensitive to the effective elastic properties (and therefore also the anisotropy index  $A^U$ ), we expect the change in effective elastic properties to be the main contributor to the separation between curves in Fig. C1d.

### C2. Effect of strut aspect ratio

To investigate the effect of strut aspect ratio  $\lambda$ , we take the struts to have elliptical cross-sections with the proportions and orientations described in Section 3.1 and vary only the cross-sectional area. The results reported in Fig. C2 indicate that the octahedron is the only architecture that exhibits a notable sensitivity to the variation in strut aspect ratio  $\lambda$ , while the other three architectures remain relatively insensitive to this geometric modification. To understand why the octahedron architecture is the most sensitive, we examine the anisotropy index  $A^U$  for each geometric variation of every pristine architecture investigated in Fig. C2, as well as the anisotropy index  $A^U$  of the imperfect architectures for a representative defect realization at a defect volume fraction of  $f = 0.15$  (see Table C2). Starting with the variation in elastic properties of the pristine architectures; the sensitivity of the anisotropy index  $A^U$  to variations in strut aspect ratio  $\lambda$  for all architectures is found to be much smaller than that which was found to be important for the tetrakaidecahedron in the prior analysis on strut cross-sectional geometry (as reported in Table C1). Furthermore, the variation in the anisotropy index  $A^U$  with respect to the strut aspect ratio  $\lambda$  is nearly identical for the octahedron and octet, confirming that the change in elastic properties from  $\lambda$  is too small to give rise to the dependency observed in Fig. C2c.

A key difference between the octahedron and octet architectures emerges when considering the change in elastic properties that occurs when defects are introduced. While the introduction of defects does not substantially alter the anisotropy

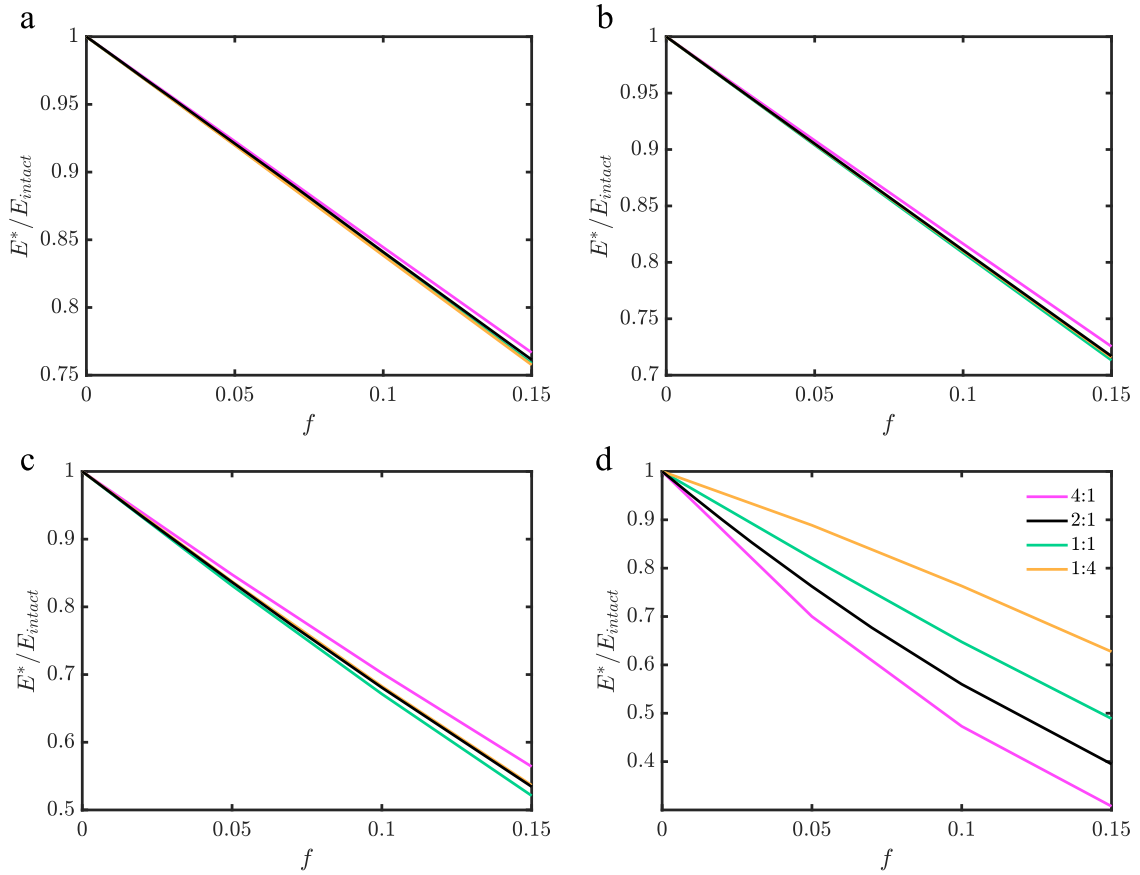


**Fig. C1.** Sensitivity of the relationship between Young’s modulus and volume fraction of randomly excluded struts to the strut cross-sectional geometry for the (a). Gurtner–Durand, (b). octet, (c). octahedron, and (d). tetrakaidecahedron architectures. The strut cross-sectional geometry is taken to be elliptical, with different proportions and orientations of the axes given by the ratio  $a_1 : a_2$ . When  $a_1 > a_2$  the major axis is aligned to the direction of loading.

**Table C1**

Elastic modulus  $E$  and anisotropy index  $A^U$  for each geometric variation of every pristine architecture investigated in Fig. C1. These values are calculated using a parent material that has an elastic modulus of 2000, a Poisson’s ratio of 0.3, and with struts that have an aspect ratio  $\lambda = 19.17$ .

Architecture	Section geometry	$E$	$A^U$
Gurtner–Durand	4:1	35.1	0.0203
	2:1	34.4	0.0180
	1:1	33.9	0.0171
	1:4	31.9	0.0203
Octet	4:1	18.0	0.477
	2:1	17.1	0.531
	1:1	16.6	0.558
	1:4	17.1	0.477
Octahedron	4:1	9.00	0.466
	2:1	8.55	0.524
	1:1	8.29	0.555
	1:4	8.56	0.466
Tetrakaidecahedron	4:1	0.358	6.21
	2:1	0.183	0.988
	1:1	0.0967	$1.58 \times 10^{-4}$
	1:4	0.0465	6.21

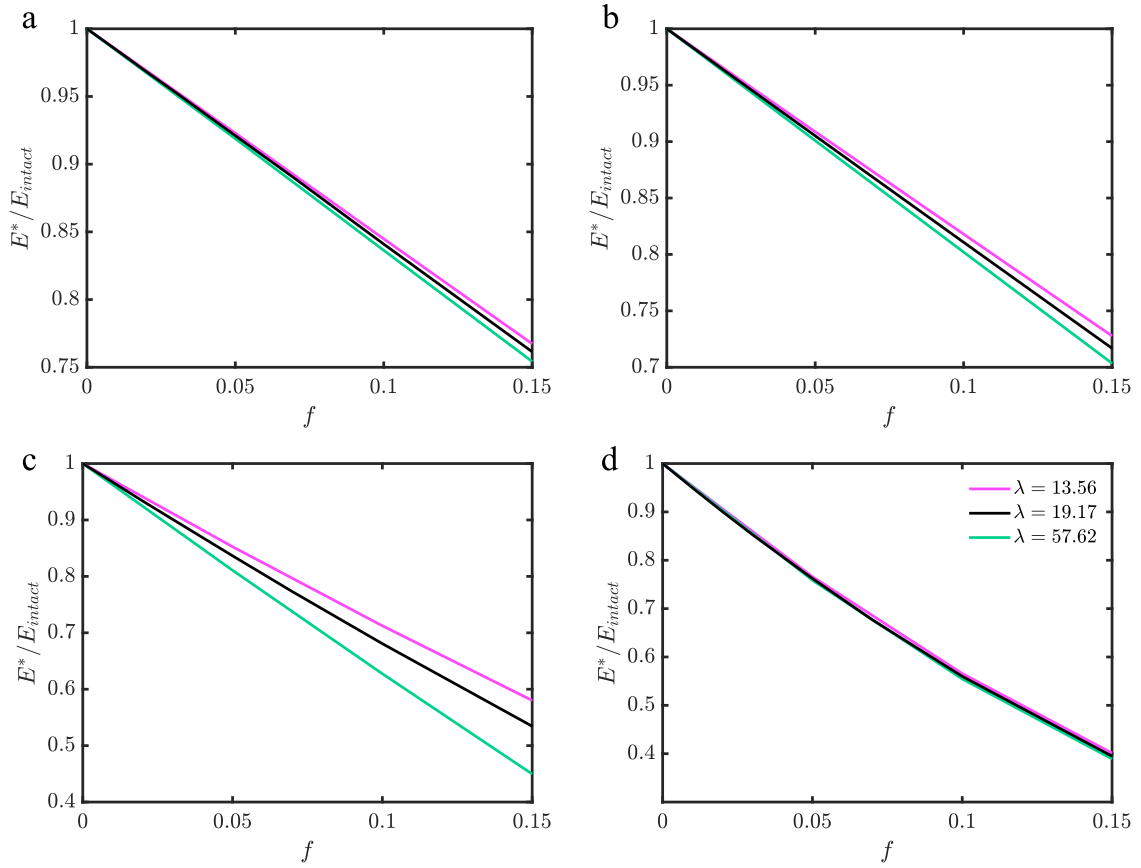


**Fig. C2.** Sensitivity of the relationship between Young’s modulus and volume fraction of randomly excluded struts to the strut aspect ratio  $\lambda$  for the (a). Gurtner-Durand, (b). octet, (c). octahedron, and (d). tetrakaidecahedron architectures.

**Table C2**

Anisotropy index  $A^U$  for each variation of strut aspect ratio  $\lambda$  investigated in Fig. C2. In addition to the results for pristine architectures, those for imperfect architectures are given as well. Imperfect results are calculated from a representative defect realization at a defect volume fraction of  $f = 0.15$ .

Architecture	$\lambda$	Pristine $A^U$	Imperfect $A^U$
Gurtner-Durand	13.56	0.0195	0.0335
	19.17	0.0180	0.0324
	57.62	0.0168	0.0316
Octet	13.56	0.478	0.470
	19.17	0.531	0.528
	57.62	0.591	0.596
Octahedron	13.56	0.465	0.394
	19.17	0.524	0.453
	57.62	0.590	0.526
Tetrakaidecahedron	13.56	0.934	0.556
	19.17	0.988	0.595
	57.62	1.041	0.633

index  $A^U$  for the octet from the pristine value, it does cause a modest shift for the octahedron. Furthermore, the degree to which anisotropy is altered for the octahedron is dependent on the strut aspect ratio  $\lambda$ . This is in contrast to the tetrakaidecahedron architecture, which also exhibits dependency of the anisotropy index  $A^U$  on the presence of defects, however for this architecture the amount that  $A^U$  changes when defects are introduced is not strongly influenced by the strut aspect ratio  $\lambda$ . For this reason, the curves in Fig. C2d are not sensitive to the strut aspect ratio  $\lambda$ , whereas the spread between the curves in Fig. C2c is expected to arise from the varying change in anisotropy that occurs for each strut aspect ratio  $\lambda$  when defects are introduced.

## Supplementary material

Supplementary material associated with this article can be found, in the online version, at doi:[10.1016/j.jmps.2018.11.007](https://doi.org/10.1016/j.jmps.2018.11.007).

## References

- Bauer, J., Schroer, A., Schwaiger, R., Kraft, O., 2016. Approaching theoretical strength in glassy carbon nanolattices. *Nat. Mater.* 15 (4), 438.
- Chen, C., Lu, T., Fleck, N., 1999. Effect of imperfections on the yielding of two-dimensional foams. *J. Mech. Phys. Solids* 47 (11), 2235–2272.
- Deshpande, V.S., Fleck, N.A., Ashby, M.F., 2001. Effective properties of the octet-truss lattice material. *J. Mech. Phys. Solids* 49 (8), 1747–1769.
- Douglas, S.M., Dietz, H., Liedl, T., Högberg, B., Graf, F., Shih, W.M., 2009. Self-assembly of DNA into nanoscale three-dimensional shapes. *Nature* 459 (7245), 414.
- Douglas, S.M., Marblestone, A.H., Teerapittayanon, S., Vazquez, A., Church, G.M., Shih, W.M., 2009. Rapid prototyping of 3D DNA-origami shapes with cad-Nano. *Nucleic Acids Res.* 37 (15), 5001–5006.
- Griffith, A.A., Eng, M., 1921. VI. The phenomena of rupture and flow in solids. *Phil. Trans. R. Soc. Lond. A* 221 (582–593), 163–198.
- Guo, X.-D.E., McMahon, T.A., Keaveny, T.M., Hayes, W.C., Gibson, L.J., 1994. Finite element modeling of damage accumulation in trabecular bone under cyclic loading. *J. Biomech.* 27 (2), 145–155.
- Guo, X.E., Gibson, L.J., 1999. Behavior of intact and damaged honeycombs: a finite element study. *Int. J. Mech. Sci.* 41 (1), 85–105.
- Gurtner, G., Durand, M., 2014. Stiffest elastic networks. *Proc. R. Soc. A* 470 (2164), 20130611.
- Hajduk, D.A., Harper, P.E., Gruner, S.M., Honeker, C.C., Kim, G., Thomas, E.L., Fetters, L.J., 1994. The gyroid: a new equilibrium morphology in weakly segregated diblock copolymers. *Macromolecules* 27 (15), 4063–4075.
- Hall, E., 1951. The deformation and ageing of mild steel: III discussion of results. *Proc. Phys. Soc. Lond. Sect. B* 64 (9), 747.
- Kanit, T., Forest, S., Galliet, I., Mounoury, V., Jeulin, D., 2003. Determination of the size of the representative volume element for random composites: statistical and numerical approach. *Int. J. Solids Struct.* 40 (13–14), 3647–3679.
- Kim, S.O., Solak, H.H., Stoykovich, M.P., Ferrier, N.J., de Pablo, J.J., Nealey, P.F., 2003. Epitaxial self-assembly of block copolymers on lithographically defined nanopatterned substrates. *Nature* 424 (6947), 411.
- Liu, X., Liang, N., 2012. Effective elastic moduli of triangular lattice material with defects. *J. Mech. Phys. Solids* 60 (10), 1722–1739.
- Lu, Z.-X., Liu, Q., Huang, J.-X., 2011. Analysis of defects on the compressive behaviors of open-cell metal foams through models using the FEM. *Mater. Sci. Eng.* 530, 285–296.
- Meza, L.R., Das, S., Greer, J.R., 2014. Strong, lightweight, and recoverable three-dimensional ceramic nanolattices. *Science* 345 (6202), 1322–1326.
- Mori, T., Tanaka, K., 1973. Average stress in matrix and average elastic energy of materials with misfitting inclusions. *Acta Metall.* 21 (5), 571–574.
- Mura, T., 2013. *Micromechanics of Defects in Solids*. Springer Science & Business Media.
- Nemat-Nasser, S., Hori, M., 2013. *Micromechanics: Overall Properties of Heterogeneous Materials*, vol. 37. Elsevier.
- Nemat-Nasser, S., Iwakuma, T., Hejazi, M., 1982. On composites with periodic structure. *Mech. Mater.* 1 (3), 239–267.
- Nemat-Nasser, S., Taya, M., 1981. On effective moduli of an elastic body containing periodically distributed voids. *Q. Appl. Math.* 39 (1), 43–59.
- Nemat-Nasser, S., Taya, M., 1985. On effective moduli of an elastic body containing periodically distributed voids: comments and corrections. *Q. Appl. Math.* 43 (2), 187–188.
- Ostoja-Starzewski, M., 2006. Material spatial randomness: from statistical to representative volume element. *Probab. Eng. Mech.* 21 (2), 112–132.
- Petch, N., 1953. The cleavage strength of polycrystals. *J. Iron Steel Inst.* 174, 25–28.
- Ranganathan, S.I., Ostoja-Starzewski, M., 2008. Universal elastic anisotropy index. *Phys. Rev. Lett.* 101 (5), 055504.
- Schaedler, T.A., Jacobsen, A.J., Torrents, A., Sorensen, A.E., Lian, J., Greer, J.R., Valdevit, L., Carter, W.B., 2011. Ultralight metallic microlattices. *Science* 334 (6058), 962–965.
- Silva, M.J., Gibson, L.J., 1997. The effects of non-periodic microstructure and defects on the compressive strength of two-dimensional cellular solids. *Int. J. Mech. Sci.* 39 (5), 549–563.
- Symons, D.D., Fleck, N.A., 2008. The imperfection sensitivity of isotropic two-dimensional elastic lattices. *J. Appl. Mech.* 75 (5), 051011.
- Van Blaaderen, A., Ruel, R., Wiltzius, P., 1997. Template-directed colloidal crystallization. *Nature* 385 (6614), 321.
- Wallach, J., Gibson, L.J., 2001. Defect sensitivity of a 3D truss material. *Scr. Mater.* 45 (6), 639–644.
- Wang, J., Li, Q., Knoll, W., Jonas, U., 2006. Preparation of multilayered trimodal colloid crystals and binary inverse opals. *J. Am. Chem. Soc.* 128 (49), 15606–15607.
- Weng, G., 1984. Some elastic properties of reinforced solids, with special reference to isotropic ones containing spherical inclusions. *Int. J. Eng. Sci.* 22 (7), 845–856.
- Winfree, E., Liu, F., Wenzler, L.A., Seeman, N.C., 1998. Design and self-assembly of two-dimensional DNA crystals. *Nature* 394 (6693), 539.
- Ye, Y.-H., LeBlanc, F., Haché, A., Truong, V.-V., 2001. Self-assembling three-dimensional colloidal photonic crystal structure with high crystalline quality. *Appl. Phys. Lett.* 78 (1), 52–54.
- Zhu, H., Knott, J., Mills, N., 1997. Analysis of the elastic properties of open-cell foams with tetrakaidecahedral cells. *J. Mech. Phys. Solids* 45 (3), 319–343.